

# Understanding the variability of nightside temperatures, NO UV and O<sub>2</sub> IR nightglow emissions in the Venus upper atmosphere

A. S. Brecht,<sup>1</sup> S. W. Bougher,<sup>1</sup> J.-C. Gérard,<sup>2</sup> C. D. Parkinson,<sup>1</sup> S. Rafkin,<sup>3</sup> and B. Foster<sup>4</sup>

Received 2 November 2010; revised 6 May 2011; accepted 23 May 2011; published 16 August 2011.

[1] Venus Express (VEX) has been monitoring key nightglow emissions and thermal features (O<sub>2</sub> IR nightglow, NO UV nightglow, and nightside temperatures) which contribute to a comprehensive understanding of the global dynamics and circulation patterns above ~90 km. The nightglow emissions serve as effective tracers of Venus' middle and upper atmosphere global wind system due to their variable peak brightness and horizontal distributions. A statistical map has been created utilizing O<sub>2</sub> IR nightglow VEX observations, and a statistical map for NO UV is being developed. A nightside warm layer near 100 km has been observed by VEX and ground-based observations. The National Center for Atmospheric Research (NCAR) Venus Thermospheric General Circulation Model (VTGCM) has been updated and revised in order to address these key VEX observations and to provide diagnostic interpretation. The VTGCM is first used to capture the statistically averaged mean state of these three key observations. This correspondence implies a weak retrograde superrotating zonal flow (RSZ) from ~80 km to 110 km and above 110 km the emergence of modest RSZ winds approaching 60 m s<sup>-1</sup> above ~130 km. Subsequently, VTGCM sensitivity tests are performed using two tuneable parameters (the nightside eddy diffusion coefficient and the wave drag term) to examine corresponding variability within the VTGCM. These tests identified a possible mechanism for the observed noncorrelation of the O<sub>2</sub> and NO emissions. The dynamical explanation requires the nightglow layers to be at least ~15 km apart and the retrograde zonal wind to increase dramatically over 110 to 130 km.

**Citation:** Brecht, A. S., S. W. Bougher, J.-C. Gérard, C. D. Parkinson, S. Rafkin, and B. Foster (2011), Understanding the variability of nightside temperatures, NO UV and O<sub>2</sub> IR nightglow emissions in the Venus upper atmosphere, *J. Geophys. Res.*, 116, E08004, doi:10.1029/2010JE003770.

## 1. Introduction

[2] After the Pioneer Venus Orbiter (PVO) mission ended in 1992 and the Magellan mission in 1994, fundamental questions still remained about our neighboring planet Venus. Currently, Venus Express (VEX) is orbiting Venus with a goal to address many of these fundamental questions and to provide a detailed study of Venus' atmosphere. This paper discusses Venus' unique global circulation and the processes that drive the variability in the upper atmosphere. Specifically, this study focuses on nightglow, a diagnostic used for understanding the upper atmosphere dynamics and global circulation. The intensity and distribution of night-

glow emissions provide information about the circulation (strength of winds and altitude variations). Nightglow emissions can be observed from Earth and spacecraft, consequently providing a proxy for the day to night flow. We will approach this question numerically with a three-dimensional (3-D) model and compare the model results to several VEX data sets.

[3] From past observations it has been noted that Venus' upper atmosphere has two dominating circulation patterns (see Figure 1) [e.g., Bougher *et al.*, 1997, 2006; Lellouch *et al.*, 1997; Schubert *et al.*, 2007]. One pattern occurs in the region between the surface of the planet to the top of the cloud deck at ~70 km. This region is dominated by a wind pattern flowing in the direction of the planets spin and is faster than Venus' rotation. This flow is known as a retrograde superrotating zonal flow (RSZ). The second pattern occurs above ~120 km and is a relatively stable mean subsolar-to-antisolar flow (SS-AS) [Bougher *et al.*, 1997]. In the upper atmosphere, Venus has inhomogeneous heating by solar radiation (EUV, UV, and IR) thus providing large pressure gradients to generate the dominant SS-AS flow pattern [Dickinson and Ridley, 1977; Schubert *et al.*, 1980; Bougher *et al.*, 1997]. In the altitude range of

<sup>1</sup>Department of Atmospheric, Oceanic, and Space Sciences, University of Michigan, Ann Arbor, Michigan, USA.

<sup>2</sup>Laboratoire de Physique Atmosphérique et Planétaire, Université de Liège, Liège, Belgium.

<sup>3</sup>Department of Space Studies, Southwest Research Institute, Boulder, Colorado, USA.

<sup>4</sup>High Altitude Observatory, National Center for Atmospheric Research, Boulder, Colorado, USA.

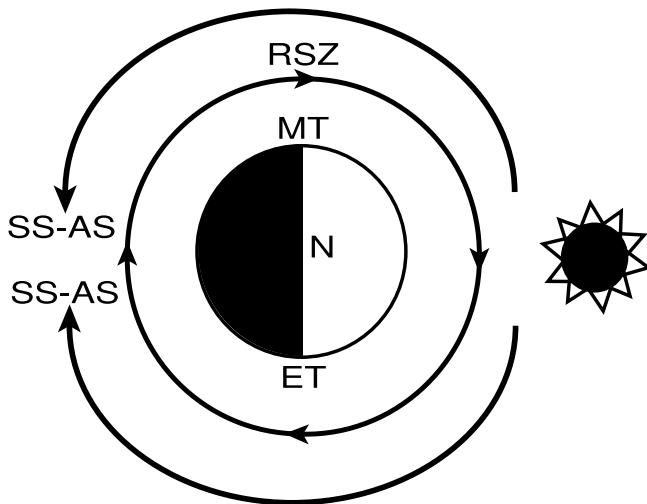


**Figure 1.** A cartoon of the Venus circulation patterns. The illustration is looking down at the north pole. MT is the morning terminator, ET is the evening terminator, SS-AS is the subsolar-antisolar wind pattern, RSZ is the retrograde superrotating zonal wind pattern. Adopted from Schubert *et al.* [2007].

70–120 km, also known as the transition region, the two major flow patterns are presumed to be superimposed; meaning both flows can be dominant in this altitude region while below this region RSZ is dominant with little evidence of a SS-AS flow and above this region SS-AS is dominant with a minor RSZ flow. Observations suggest a high degree of variability of these wind components in the transition region.

[4] This interaction produces at least three modifications to the general flow in the upper atmosphere: (1) a shift in the divergence of the flow from the subsolar point toward the morning terminator, (2) stronger evening terminator winds than those along the morning terminator, and (3) a shift in the convergence of the flow away from midnight and toward the morning terminator [Schubert *et al.*, 2007]. These modifications also vary with altitude which reflects the changing importance of underlying drivers and solar cycle variations. The specific processes responsible for maintaining and driving variations in the SS-AS and RSZ wind components in Venus' upper atmosphere are still not well understood or quantified. More importantly, the interaction between the two flows occurs in a region where there is limited spacecraft and ground based data and for which modeling is most challenging.

### 1.1. Pre VEX Data Sets

[5] These characteristics of Venus' upper atmosphere dynamics have been gleaned from a number of remote and in situ data sets collected at the planet. A thorough examination of PVO neutral density (e.g., CO<sub>2</sub>, O, He, and H) and temperature distributions above ~130 km has been used to constrain general circulation model simulations, from which SS-AS and RSZ wind magnitudes can be extracted (see reviews by Bougher *et al.* [1997] and see Bougher *et al.* [2006, Table 1]). The spatial distribution of PVO ultraviolet (UV) night airglow emissions (e.g., NO), PVO UV

dayglow emissions (e.g., atomic O), and H-Lyman- $\alpha$  emissions, have all been used to trace the circulation patterns at thermospheric altitudes above ~115 km. Visible and infrared (IR) O<sub>2</sub> nightglow distributions from Veneras 9 and 10, Galileo, PVO and the ground, along with minor species distributions (especially CO) have also been used to constrain upper mesospheric wind patterns (~80–110 km) (see review by Lellouch *et al.* [1997]). Many of these data sets are discussed in detail by Bougher *et al.* [1997], Lellouch *et al.* [1997], and Schubert *et al.* [2007]. See summary of Bougher *et al.* [2006, Table 1] for more detailed information.

[6] Connes *et al.* [1979] were the first to observe O<sub>2</sub> IR night airglow at 1.27  $\mu\text{m}$  by using a ground-based Fourier transform spectrometer. Recent ground-based observations have been performed by Crisp *et al.* [1996], Ohtsuki *et al.* [2005, 2008], and Bailey *et al.* [2008]. Crisp *et al.* [1996] documented, from 1990 to 1994, the O<sub>2</sub> nightglow peak emission ranging from 0.5 MR to 6 MR (MR = megarayleigh =  $10^{12}$  photons  $\text{cm}^{-2} \text{s}^{-1}$  into  $4\pi$  sr) with a nightside-averaged emission rate near 1 MR. The bright regions varied spatially and temporally, but on average occurred in lower latitudes between local times of 00:00 and 03:00 LT. The nightglow observations yielded a rotational temperature of  $186 \pm 6$  K in the altitude range of 90–115 km. Ohtsuki *et al.* [2005, 2008] had three different observation periods (2002, 2004, 2005) and observed peak emissions from 1 to 3 MR with the bright region near the antisolar point but varied day to day. Their average rotational temperatures from these nightglow observations were  $193 \pm 9$  K,  $182 \pm 25$  K, and  $185 \pm 20$  K, which also showed an association with the nightglow patches of the peak emission. Bailey *et al.* [2008] observed during two different time sequences in 2004 and 2005 and discerned the peak emission to range from 1.5 to 4.8 MR with the bright region occurring in low latitudes around the antisolar point but occasionally had a displacement of ~2 hours toward the morning terminator. They derived temperatures from 181 to 196 K and also showed the connection of warmer temperatures with the nightglow patches. From these few ground observations, a basic understanding of the dynamics in the upper mesosphere/lower thermosphere region where the O<sub>2</sub> nightglow occurs was developed.

[7] The NO UV night airglow provides information higher in the atmosphere. The NO UV nightglow peak layer is observed in a range from ~95–132 km. The NO UV nightglow consists of  $\delta$  (190–240 nm) and  $\gamma$  (225–270 nm) bands and was observed first by two different groups; Feldman *et al.* [1979] and Stewart and Barth [1979]. Feldman *et al.* [1979] detected the nightglow with the ultraviolet spectrograph on the International Ultraviolet Explorer (IUE), while Stewart and Barth [1979] used the ultraviolet spectrometer on PVO. Stewart *et al.* [1980] provided images only for the strongest  $\delta$  (0, 1) band from Pioneer Venus. The observations suggested large day-to-day variations and the peak emission regions varied in intensity and location. Stewart *et al.* [1980] stated that, on average, the nightglow peak for the  $\delta$  (0, 1) band was located near 02:00 local time (LT) and slightly south of the equator. The average peak emission rate for the bright region, after revision by Bougher *et al.* [1990], was determined to be ~1.9 kR (kR = kilorayleigh) for the  $\delta$  (0, 1) band. Gérard *et al.* [1981] determined the altitude of the

peak emission to be near  $115 \pm 2$  km from PVO limb observations near periaapsis. The NO UV and O<sub>2</sub> IR nightglows are consistently observed in the transition region of the Venus upper atmosphere. Other observations from VEX will be discussed in section 1.2.

[8] In addition, PVO made a surprising discovery about Venus' thermospheric temperatures. Temperatures on the dayside at 100 km are  $\sim 180$  K and increase to  $\sim 300$  K at the exobase; on the nightside temperatures are  $\sim 180$  K at 100 km and decrease to  $\sim 100$ – $120$  K at the exobase [Schubert *et al.*, 1980; Bougher *et al.*, 1997]. This unusual nightside upper atmosphere region ( $>100$  km) has been designated as the Venus "cryosphere" [Keating *et al.*, 1979; Schubert *et al.*, 1980]. The reasons for the existence of the cryosphere have been examined using hydrodynamic models [Bougher *et al.*, 2006; Schubert *et al.*, 2007].

[9] Venus' rotation is very slow with its day being longer than its year, giving rise to large day-night pressure gradients and very strong SS-AS winds. By using nominal input parameters, the upper atmospheric winds were simulated yielding higher flow speeds than inferred from these data sets (spacecraft and ground based). These simulations produced much too warm nightside temperatures due to compressional heating [Dickinson and Ridley, 1977; Schubert *et al.*, 1980]. Thus there is evidence of a decelerating mechanism needed to model the winds appropriately [e.g., Alexander, 1992; Zhang *et al.*, 1996; Bougher *et al.*, 1997]. Understanding how the atmosphere is decelerated is important since the net day-to-night upper atmosphere circulation, above 90 km, produces nightside downwelling and is crucial for maintaining the observed cold nightside temperatures ( $\sim 100$ – $120$  K) and the measured density structure. The deceleration mechanism is likely not symmetric in local time, since the net zonal winds appear stronger at the evening terminator than the morning terminator [Bougher *et al.*, 1997].

[10] Lastly, ground-based wind measurements have been made using several different techniques; CO<sub>2</sub> 10  $\mu\text{m}$  infrared heterodyne spectroscopy, CO millimeter and submillimeter measurements, CO emission lines at 4.7  $\mu\text{m}$ , and visible observations of reflected solar lines. For brevity, only a few observations are discussed, and the reader is referred to Lellouch *et al.* [1997, Table 1] and Bougher *et al.* [2006, Table 1] for more details.

[11] Goldstein *et al.* [1991] observed (December 1985 and March 1987) absolute wind velocities near  $110 \pm 10$  km altitude using the CO<sub>2</sub> 10  $\mu\text{m}$  infrared heterodyne spectroscopy technique. The observations provided a SS-AS circulation near  $120 \pm 30$  m s<sup>-1</sup> along with a small superimposed RSZ wind component of  $25 \pm 15$  m s<sup>-1</sup>. At slightly lower altitudes ( $\sim 99$  km) CO J(0-1) millimeter measurements were made during late April and early May 1988 by Shah *et al.* [1991]. At these times, strong RSZ wind speeds of  $\sim 130 \pm 10$  m s<sup>-1</sup> were dominant, while the SS-AS wind was very small. Other observations have been made, specifically by the CO lines at 4.7  $\mu\text{m}$  which calculated a total wind (zonal wind +  $0.7 \times$  SS-AS)  $140 \pm 45$  and  $200 \pm 50$  [Maillard *et al.*, 1995].

## 1.2. VEX Era Observations

[12] In order to understand the upper atmosphere dynamics and circulation patterns on Venus, ongoing

monitoring of night airglow intensities and distributions has been conducted. New VEX observations have begun augmenting this record with measurements of key nightglow distributions (e.g., NO, O<sub>2</sub>) and vertical structure measurements, both contributing to a growing climatology of the inferred SS-AS and RSZ wind variations [Bougher *et al.*, 2006; Svedhem *et al.*, 2009].

[13] There are two specific instruments on VEX that focus on these measurements in this region: Spectroscopy for Investigation of Characteristics of the Atmosphere of Venus (SPICAV) and Visible and InfraRed Thermal Imaging Spectrometer (VIRTIS). SPICAV is an instrument with three different spectrometers; UV (110–310 nm), VIS-IR (0.7–1.7  $\mu\text{m}$ ), and solar occultation IR (SOIR) (2.2–4.3  $\mu\text{m}$ ). The SPICAV UV spectrometer provides night airglow (nadir and limb) observations of NO (190–270 nm) emissions, which contribute to the creation of statistical maps. Furthermore, SPICAV provides repeated measurements of vertical profiles of atmospheric density (and inferred temperatures) over  $\sim 80$ – $180$  km (dayside) and  $\sim 80$ – $150$  km (nightside) via stellar and solar occultations [Bertaux *et al.*, 2007]. VIRTIS is an imaging spectrometer with three channels: VIRTIS-M-VIS (imager; 0.3–1  $\mu\text{m}$ ), VIRTIS-M-IR (imager; 1–5  $\mu\text{m}$ ), and VIRTIS-H (high-resolution; 2–5  $\mu\text{m}$ ). Its observations address upper atmosphere dynamics by (1) measuring the 3-D temperature and derived thermal wind fields ( $\sim 60$ – $90$  km) on the nightside and (2) mapping the O<sub>2</sub> IR nightglow at 1.27  $\mu\text{m}$  as a tracer of the wind system over  $\sim 90$  to 130 km. Repeated measurements over several orbits provide a monitor of the IR nightglow variability at different time scales [Drossart *et al.*, 2007].

### 1.2.1. Temperature

[14] An important diagnostic for upper atmosphere dynamics is the thermal structure, which is gradually being revealed by VEX. A distinctly warm layer on the nightside ( $\sim 100$  km) has been discovered by stellar occultation measurements with the SPICAV instrument [Bertaux *et al.*, 2007]. The SPICAV observations suggest the temperatures between 95 and 100 km are highly variable, with an observed temperature range of  $\sim 185$  K to  $\sim 240$  K. An estimated corresponding vertical velocity was calculated to be near  $-0.43$  m s<sup>-1</sup>. These authors state that continued measurements are needed to establish a climatology of these temperatures and confirm a representative mean value in this nightside altitude region.

[15] The Venus Express Radio Science (VeRa) observations provide temperature profiles and temperature maps of the mesosphere (below  $\sim 90$  km and above  $\sim 50$  km) [Pätzold *et al.*, 2007]. VIRTIS has measured dayside CO<sub>2</sub> nonlocal thermodynamic equilibrium (NLTE) emission at 4.3  $\mu\text{m}$  up to 160 km and 2.7  $\mu\text{m}$  up to 130 km. In addition, CO NLTE emission has been observed at 4.3  $\mu\text{m}$  up to 120 km [López-Valverde *et al.*, 2007; Drossart *et al.*, 2007; Gilli *et al.*, 2009].

[16] Ground-based observations have recently shown significant variations in nightside temperatures for the 95–100 km region. Rengel *et al.* [2008] published preliminary submillimeter measurements of CO as part of a ground-based observing campaign in support of VEX and MESSENGER. This study compared a single temperature profile from one observation (8 June 2007) with past nightside temperature profiles and Bertaux *et al.* [2007] profiles. The Rengel *et al.* [2008] measurement of  $\sim 185$  K at 100 km is

consistent with the lower range of *Bertaux et al.*'s [2007] observations. *Clancy et al.* [2008] also performed submillimeter line measurements of CO in support of the VEX and MESSENGER ground-based observation campaigns. Over four days (2 June, 3 June, 6 June, and 11 June 2007) of observations, *Clancy et al.*'s [2008] limb profiles near the equator at 20:30 LT show temperatures ranging from 170 to 175 K near 100 km. These temperatures are much cooler than those of *Bertaux et al.* [2007] and *Rengel et al.* [2008]. *Clancy et al.* [2008] suggests the temperature increase is caused by a diurnal radiative balance, while *Bertaux et al.* [2007] suggests the localized warming is due to localized compressional heating from the downwelling of the day to night circulation.

[17] *Bailey et al.* [2008] created nightside temperature maps from O<sub>2</sub> ( $a^1\Delta_g$ ) night airglow observations with the Anglo-Australian Telescope. Their results also show night-to-night variations. For 3 days in July 2004, the intensity weighted mean temperature ranged from 195 to 196 K at  $\sim 97$  km. During three other days in December 2005, the intensity weighted mean temperature varied from 181 to 190 K at  $\sim 97$  km. *Bailey et al.* [2008] provides a summary of available nightside temperature measurements at  $\sim 95$  km, which has been adopted in this study as Table 5. Furthermore, *Ohtsuki et al.* [2005, 2008] derived nightside temperatures from O<sub>2</sub> IR nightglow. They observed temperatures ranging from  $\sim 183$  to  $\sim 193$  K near 95 km. Both *Bailey et al.* [2008] and *Ohtsuki et al.* [2008] observe a correlation between the nightside warm layer and the peak O<sub>2</sub> IR nightglow. They made rough estimates of the vertical velocities needed to produce the warm temperature in this region; *Bailey et al.* [2008] calculated  $-0.2$  m s<sup>-1</sup> and *Ohtsuki et al.* [2008] calculated  $-0.05$  m s<sup>-1</sup>. Both estimates are consistent with *Bertaux et al.* [2007] observations leading them to the same conclusion; the nightside temperature enhancement is due to localized compressional heating of downwelling gas from the global thermospheric circulation. With these observations, a possible range of variability of the nightside temperatures in the upper mesosphere can be assembled.

[18] The Venus International Reference Atmosphere (VIRA), a model based on PVO Infrared Radiometer (OIR) and probe deceleration data, gives a temperature of 168 K at 95 km [*Seiff et al.*, 1985] for latitude  $<30^\circ$ . This is much cooler than what is currently being observed. However, it should be noted that VIRA is a diurnally averaged empirical model making use of only a few profiles from select probe locations. Furthermore, *Seiff et al.* [1985] state that above 95 km a diurnally averaged model will only be accurate within 10 K.

### 1.2.2. Night Airglow

[19] Nightglow distribution maps provide important constraints in modeling Venus' atmospheric dynamics. Sufficient observations from 16 May 2006 to 7 April 2007 (1225 images) were used to create an averaged statistical map (averaged spatially and temporally) of the O<sub>2</sub> IR night airglow [*Gérard et al.*, 2008b]. Their results show the maximum emission near  $\sim 3$  MR and the mean hemispheric vertical intensity at 1.3 MR. The limb observations indicate a production peak for the nightglow near 96 km but the peak can range from  $\sim 90$  to 110 km. Due to the trajectory of VEX, the southern hemisphere is mainly sampled for the O<sub>2</sub>

IR night airglow. Nevertheless, previous observations discussed in section 1.1 strongly indicate the nightglow to concentrate near the equator at midnight. Recently, *Soret et al.* [2011] recompiled the VIRTIS-M data and merged the nadir and the limb O<sub>2</sub> nightglow observations. Their results confirm that the bright spot is statistically centered near midnight on the equator. It has a maximum local intensity of 1.6 MR and a hemispheric average of 0.47 MR. These values are less than published by *Gérard et al.* [2008b], who subtracted a smaller amount of thermal background emission at 1.27  $\mu\text{m}$  from the nadir observations. The mean value for the O peak density derived from the Abel inversion of the O<sub>2</sub> emission limb profiles is about  $2 \times 10^{11}$  cm<sup>-3</sup> with a mean altitude of 103–104 km [*Gérard et al.*, 2009a; *Soret et al.*, 2011]. Individual limb profiles revealed the O density peak altitude to range between 95 and 115 km and the density peak to vary between 1 and  $5 \times 10^{11}$  cm<sup>-3</sup>.

[20] Alternatively, *Piccioni et al.* [2009] used VIRTIS limb measurements from 42 orbits to study the statistical characteristics of the 1.27  $\mu\text{m}$  emission. From the analyzed retrieved profiles, the peak altitude of the volume emission rate is observed between 95 and 100 km with a mean of  $97 \pm 2.5$  km. This is very similar to that of *Gérard et al.* [2010], who analyzed 1843 limb profiles and found an average peak brightness along the line of sight of  $28 \pm 23$  MR at  $96 \pm 2.7$  km. In addition, a mean total vertical emission rate was calculated as 0.52 MR [*Piccioni et al.*, 2009]. *Piccioni et al.* [2009] constructed a distribution map from 880 orbits with observations that had emergence angles less than  $80^\circ$ . The localized peak vertical emission rate was 1.2 MR located at midnight and was slightly south of the equator. While the mean total vertical emission rate is very similar to the hemispheric average value from *Soret et al.* [2011], the localized peak intensity is reduced but within ranges previously observed. Finally, from visually tracking the O<sub>2</sub> IR nightglow brightest features, mean zonal and meridional velocities can be estimated [*Hueso et al.*, 2008].

[21] The NO Ultraviolet (UV) night airglow has been measured by SPICAV, the UV spectrometer, thus far with rather limited spatial and temporal coverage. Statistical mean maps (composed of spatially and temporally averaged observed emissions) of the NO nightglow are presently being constructed [*Cox*, 2010]. SPICAV has made limb observations in both the  $\delta$  (190–240 nm) and  $\gamma$  (225–270 nm) bands. For *Gérard et al.* [2008c], only 17 SPICAV orbits and 201 SPICAV limb scans have been obtained providing acceptable NO UV night airglow limb profiles. These orbits already show large fluctuations in emission intensity and location. Early results from nadir observations with SPICAV [*Cox*, 2010] confirm the pattern previously observed at solar maximum with Pioneer Venus, (i.e., the statistically averaged NO UV nightglow emission peaks near the equator around 02:00 LT) [*Stewart et al.*, 1980].

[22] VEX observations have begun to characterize the variability of the two (O<sub>2</sub> IR and NO UV) nightglow layers (i.e., both horizontal and vertical distributions) [*Hueso et al.*, 2008; *Piccioni et al.*, 2008; *Gérard et al.*, 2008b, 2008c, 2009a, 2009b, 2010]. The O<sub>2</sub> nightglow statistical bright emission has been observed from 95 to 105 km, ranging from 22:00 to 01:00 LT, at latitudes from  $30^\circ\text{N}$  to  $20^\circ\text{S}$ , with corresponding varying vertical intensities 0.5 MR to

3 MR. The NO nightglow has been observed from 95 to 132 km, ranging from 22:00 to 03:00 LT, located at 30°S to 60°N, with varying vertical intensities of 1–6 kR. These changes have been seen on very short timescales. See sections 4.2 and 4.3 for more discussion of the observed variability.

[23] Furthermore, *Gérard et al.* [2009b] have shown the first concurrent observations of the O<sub>2</sub> IR and NO UV night airglow with VIRTIS and SPICAV data. They concluded that the two nightglow emissions are not spatially correlated, giving rise to the idea that each emission is controlled by different dynamical processes [*Collet et al.*, 2010]. Recent publications [*Gérard et al.*, 2008b, 2008c, 2009a, 2009b, 2010; *Bertaux et al.*, 2007; *Piccioni et al.*, 2009] detailing observations made by these instruments are discussed in section 4.

[24] Finally, the OH IR nightglow on Venus was first observed with VIRTIS on VEX by *Piccioni et al.* [2008]. The Meinel bands of (1-0) at 2.8  $\mu\text{m}$ , (2-1) at 2.94  $\mu\text{m}$ , and (2-0) at 1.43  $\mu\text{m}$  were identified with evidence of additional bands in the  $\Delta v = 1$  sequence. Due to the weak emission, the nightglow is only observed at the limb. The limb intensity for the (1-0) band was  $0.88 \pm 0.09$  MR located at  $96 \pm 2$  km [*Piccioni et al.*, 2008]. Additionally, *Krasnopolsky* [2010] observed the OH IR nightglow for the first time from the ground. He observed the (1-0) P1(4.5) line at 2.8  $\mu\text{m}$  and (2-1) Q1(1.5) line at 2.94  $\mu\text{m}$  nightglow lines. The observed slant intensities at 21:30 LT were  $7.2 \pm 1.8$  kR and  $<1.4$  kR, respectively. Furthermore, at 04:00 LT the intensities were  $15.5 \pm 2$  kR and  $4.7 \pm 1$  kR, respectively. Both of these OH IR nightglow emissions peaked near 100 km.

[25] The VEX OH IR data has been studied by *Gérard et al.* [2010] for correlations between the OH ( $\Delta v = 1$ ) and the O<sub>2</sub> IR nightglow emissions and also by *Soret et al.* [2010] to determine the global distribution of OH ( $\Delta v = 1$ ). *Gérard et al.* [2010] conducted a preliminary study and found an average brightness near  $0.41 \pm 0.37$  MR peaking at  $95.3 \pm 3$  km. A correlation with the O<sub>2</sub> IR nightglow was noted. More recently, *Soret et al.* [2010] has utilized 3328 limb profiles to find a mean peak of the OH ( $\Delta v = 1$ ) emission of  $0.35_{-0.21}^{+0.53}$  MR with a location near  $96.4 \pm 5$  km. The intensity is highly variable; i.e., it has been observed as low as  $<20$  kR and as high as 2 MR [*Soret et al.*, 2010]. In addition, the intensity tends to be higher near the antisolar point rather than toward the poles. *Soret et al.* [2010] also noted a correlation of the OH IR and the O<sub>2</sub> IR nightglow emissions. This is anticipated since both nightglows production mechanisms are dependent on the same reactant, atomic O, which is created on the dayside and transported to the nightside by the global wind system.

### 1.2.3. Wind Observations

[26] The cloud morphology is also being monitored by VIRTIS and the Venus Monitoring Camera (VMC) in the UV to help provide more information about the dynamics of Venus' atmosphere. Sequences of images are being used to track the motions of cloud features. Derived wind speeds near the cloud tops (50–70 km) can be deduced from the motion of cloud features [*Markiewicz et al.*, 2007; *Sánchez-Lavega et al.*, 2008; *Moissl et al.*, 2009]. The VIRTIS instrument made wind measurements from cloud tracking at

three different altitudes layers in the Southern hemisphere. At the cloud tops ( $\sim 66$  km), near low latitudes, the zonal winds were measured to be westward at  $105 \text{ m s}^{-1}$  and nearly constant with respect to latitude [*Sánchez-Lavega et al.*, 2008]. The cloud base ( $\sim 47$  km) winds were measured to be  $60\text{--}70 \text{ m s}^{-1}$ . The zonal winds at higher latitudes decreased poleward and values were lower than  $15 \text{ m s}^{-1}$  [*Sánchez-Lavega et al.*, 2008]. The more recent discussion by *Moissl et al.* [2009] used observations from VMC and VIRTIS. *Moissl et al.* [2009] claimed, at latitudes poleward of 60°S, winds are difficult to track because of low contrast and scarcity of features. However, they continue to collect data and extend the latitudinal coverage [*Moissl et al.*, 2009].

[27] Alternatively, *Sornig et al.* [2008] used the CO<sub>2</sub> 10  $\mu\text{m}$  infrared heterodyne spectroscopy technique in 2007 and made ground-based observations at the equator and at higher latitudes along the west limb (subsolar meridian). At the equator near 110 km, weak RSZ winds were measured ( $3 \pm 7 \text{ m s}^{-1}$ ) while stronger zonal winds were obtained at higher latitudes ( $32 \pm 4 \text{ m s}^{-1}$ ). They also retrieved a smaller SS-AS wind ( $52 \pm 18 \text{ m s}^{-1}$ ) compared to previous measurements by *Goldstein et al.* [1991]. *Clancy et al.* [2008] used CO submillimeter measurements to derive zonal winds over an altitude range of  $\sim 80\text{--}110$  km. Due to their observing geometry, they were unable to separate the RSZ and SS-AS components, but derived total zonal winds of  $195 \pm 70$  and  $235 \pm 70 \text{ m s}^{-1}$  from two observing days in a latitude range of 30°S–30°N at the evening terminator (14:00–22:00 LT). Another method used to measure the winds of Venus from Earth makes use of visible Fraunhofer line scattering by Venus' cloud tops, which *Widemann et al.* [2008] used to obtain measurements at the equator and near 68 km. Their mean wind speed, averaged over four days, of the zonal winds at the cloud tops was  $104 \pm 10 \text{ m s}^{-1}$ . This velocity is consistent with UV cloud tracking measurements.

[28] Overall, it can be discerned from the available wind measurements the RSZ winds decrease on average from the cloud tops to  $\sim 110$  km. However there are large variations in the RSZ winds over 70–110 km altitude range. By examining observations near the cloud top region (60–70 km), an average zonal wind velocity is  $\sim 100 \text{ m s}^{-1}$ . Investigating the altitude range of  $\sim 100$  to 105 km, both RSZ and SS-AS winds are highly variable, ranging from  $\sim 0$  to  $130 \text{ m s}^{-1}$  and up to  $300 \text{ m s}^{-1}$ , respectively. At 110 km, the general trend shows the RSZ winds are present but are usually weak, while the SS-AS winds are  $\sim 120 \text{ m s}^{-1}$ . This provides strong evidence of Venus' highly varying winds and complex dynamics between  $\sim 70$  km and 110 km. It is important to obtain wind measurements at various local times in order to validate global circulation models, which help to provide a better overall understanding of Venus' upper atmosphere. More information on ground-based wind measurements is given by *Lellouch et al.* [1997], *Bougher et al.* [2006], and *Sornig et al.* [2008].

### 1.2.4. Wave Observations

[29] Perturbations in density, temperature, and cloud structures are observed by VEX and are thought to be caused by a source of variability in Venus' upper atmosphere. The actual source of these perturbations is unknown; however gravity waves are commonly implicated. Specifically, VIRTIS has detected perturbations in CO<sub>2</sub> NLTE

4.3  $\mu\text{m}$  emissions [Garcia *et al.*, 2009]; where this emission originates in an altitude range of  $\sim 110$  km to 140 km. From these observations they are able to obtain wave structures with horizontal wavelengths ranging from 90 to 400 km. Additionally, derived horizontal phase velocities (magnitude and direction) are consistent between orbits and are on average of  $70 \text{ m s}^{-1}$  westward and  $30 \text{ m s}^{-1}$  northward [Garcia *et al.*, 2009]. Garcia *et al.* [2009] claim these observed waves are generated from the polar vortex. Moreover, VIRTIS and VMC observed visible trains of oscillating cloud brightness in the UV for an upper cloud layer ( $\sim 66$  km) on the dayside and from thermal radiation for the lower cloud layer on the nightside [Peralta *et al.*, 2008]. Wavelengths and phase speeds are also derived from these observations. Peralta *et al.* [2008] observed wavelengths of 60–150 km, which propagate westward with phase velocities similar to the zonal flow and are confined to horizontal wave packets of 400 to 1800 km. They find no correlation between the waves and surface topography, latitude, LT, or wind structure. The perturbations in these observations help provide information on potential waves mechanisms in Venus' atmosphere.

### 1.3. This Study

[30] This study is focused upon general circulation model (GCM) analysis and interpretation of select recent observations from VEX. The selected nightglow emissions are O<sub>2</sub> IR (1.27  $\mu\text{m}$ ) and NO UV (190–270 nm); they serve as effective tracers of Venus' middle and upper atmosphere circulation due to their brightness. Nightside temperatures are also an important diagnostic for the circulation of the upper atmosphere. The National Center for Atmospheric Research (NCAR) Venus Thermospheric General Circulation Model (VTGCM) will be utilized, since it now spans the altitude range appropriate for these night airglow emissions,  $\sim 70$ –200 km, on the nightside. The VTGCM has been updated and revised to produce results that are similar to upper atmosphere observations and other 1-D models.

[31] The first objective of this study will be to define, with the available VEX data, a “mean” state for the nightside temperatures and the two nightglow emissions. The “mean” state will then be illustrated with corresponding global VTGCM simulations. Moreover, we will describe in detail how the VTGCM is used to examine the connections between the changing dynamical flows and the averaged nightglow and thermal features. The second objective (using the VTGCM “mean” state) is to examine possible processes which may control the variability of the night airglow distributions (both horizontal and vertical) and temperatures near 100 km. The possible processes in the VTGCM are addressed using tunable parameters (the nightside eddy diffusion coefficients and the magnitude of wave drag) and two uncertain chemical reaction rates. These parameters are varied to examine how they impact the night airglow features and the global dynamics. Ultimately, these sensitivity tests will help provide a better understanding of the processes driving the variability in Venus' atmospheric dynamics.

[32] Section 2 of this paper discusses the VTGCM (including its recent upgrades) in detail. Section 3 describes the results of the VTGCM simulations, which is followed

by a discussion about the model results, comparison with new VEX data sets, and their implications for dynamical processes (section 4). Finally, section 5 contains the main conclusions.

## 2. Model Description and Implementation

### 2.1. Model Description

[33] The VTGCM is a 3-D, fourth-order, centered finite difference, hydrodynamic model of the Venus upper atmosphere [e.g., Bougher *et al.*, 1988] which is based on the NCAR terrestrial Thermospheric Ionosphere General Circulation Model (TIGCM). VTGCM revisions and improvements have been documented over nearly 2 decades [see Bougher *et al.*, 1988, 1990, 1997, 1999, 2002, 2008; Bougher and Borucki, 1994; Zhang *et al.*, 1996]. The VTGCM code has recently been reconstructed on a new computer platform, the NCAR IBM/SP super computers [Brecht *et al.*, 2007, 2009]. This new VTGCM code makes efficient use of 4 to 32 processors in a multitasking environment. A parallel dynamical solver is implemented, for which assigned 2-D (latitude versus longitude) blocks spanning all altitudes are distributed over the globe (and these processors) to reduce the overall clock time for calculations. The new VTGCM has the capability of modeling both hemispheres, instead of mirroring one to the other, enabling small Venus seasonal effects to be simulated. Subroutines from the previous VTGCM code [see Bougher *et al.*, 1988, 1990; Bougher and Borucki, 1994] are modified to accommodate the new array structure. The EUV-UV heating, ionization, and dissociation routines are now based on a slant column integration scheme that is optimized; this routine is called every model time step.

[34] The VTGCM solves the time-dependent primitive equations for the neutral atmosphere. The diagnostic equations (hydrostatic and continuity) provide geopotential and vertical motion. Additionally, the prognostic equations (thermodynamic, eastward momentum, northward momentum, and composition) are solved for steady state solutions for the temperature, zonal (eastward) velocity, meridional (northward) velocity, and mass mixing ratio of specific species. The VTGCM composition includes major species (CO<sub>2</sub>, CO, O, and N<sub>2</sub>), minor species (O<sub>2</sub>, N(<sup>4</sup>S), N(<sup>2</sup>D), and NO), and dayside photochemical ions (CO<sub>2</sub><sup>+</sup>, O<sub>2</sub><sup>+</sup>, O<sup>+</sup>, and NO<sup>+</sup>). These equations have been described in detail by Bougher *et al.* [1988]; primed (perturbation) values have now been replaced by total field values. The model covers a 5° by 5° latitude-longitude grid, with 69 evenly spaced log pressure levels in the vertical from  $z_p = -16$  to  $z_p = 18$  ( $z_p = \ln(P_o/P)$ ;  $P_o = 5 \times 10^{-3} \mu\text{ bar}$ ), and extending from approximately  $\sim 70$  to 300 km ( $\sim 70$  to 200 km) at local noon (midnight). The latitudinal points are placed at  $\pm 2.5^\circ$  to  $\pm 87.5^\circ$  in both directions (north and south). Currently, a 30 s time step is utilized for all new VTGCM simulations to satisfy the Courant-Friedrichs-Lewy (CFL) stability criterion. Dayside O and CO sources arise primarily from CO<sub>2</sub> net dissociation and ion-neutral chemical reactions. The VTGCM ion-neutral chemistry is updated based upon the chemical reactions and rates of Fox and Sung [2001]. The model can be used to examine Venus' thermospheric structure and winds from solar maximum to solar minimum

EUV-UV flux conditions. In addition, the VTGCM is designed to calculate O<sub>2</sub> IR (1.27  $\mu\text{m}$ ) [Bougher and Borucki, 1994] and NO UV ( $\delta$  band 190–290 nm and  $\gamma$  band 225–270 nm) [Bougher et al., 1990] nightglow distributions for comparison with various Venera, PVO, VEX, and ground-based measurements (see section 2.2.3 for more details on the nightglow calculation assumptions).

## 2.2. Model Implementation

### 2.2.1. CO<sub>2</sub> 15 $\mu\text{m}$ Cooling, Wave Drag, and Eddy Diffusion

[35] Formulations for CO<sub>2</sub> 15  $\mu\text{m}$  cooling, wave drag, and eddy diffusion are incorporated into the VTGCM [e.g., Bougher et al. 1988]. CO<sub>2</sub> 15  $\mu\text{m}$  emission is known to be enhanced by collisions with O atoms, providing increased cooling in NLTE regions of the upper atmosphere [see Bougher et al., 1994; Kasprzak et al., 1997]. The corresponding collisional relaxation rate adopted for typical benchmark VTGCM simulations is  $3 \times 10^{-12} \text{ cm}^3 \text{ s}^{-1}$  at 300 K [Bougher et al., 1999]. This value provides strong CO<sub>2</sub> 15  $\mu\text{m}$  cooling that is consistent with the use of EUV-UV heating efficiencies of ~20–22%, which are in agreement with detailed offline heating efficiency calculations of Fox [1988].

[36] Subgrid scale processes (i.e., eddy diffusion, viscosity, conduction, and wave drag) are not self-consistently formulated in the VTGCM, but rather parameterized using standard aeronautical formulations. For instance, Rayleigh friction is adopted to parameterize wave drag effects on the mean flow; this drag is thought to result from gravity wave momentum deposition. In particular,  $F_{\text{drag}} = \lambda_{RF} (u - u_{SR})$  where  $\lambda_{RF}$  is a wave drag damping rate,  $u$  is the calculated zonal wind, and  $u_{SR}$  is the specified zonal wind speed to approximate the RSZ wind [Bougher et al., 1988]. The maximum  $u_{SR}$  value is set to  $75 \text{ m s}^{-1}$ . The wave drag damping rate is expressed as  $\lambda_{RF} = \lambda_o \sqrt{P_{\text{break}}/P}$ , where  $\lambda_o$  is the maximum  $\lambda_{RF}$  ( $\lambda_o = 0.5 \times 10^{-4} \text{ s}^{-1}$ ) and  $P_{\text{break}}$  is the breaking level ( $P_{\text{break}} = 2.24 \times 10^{-2} \mu \text{ bar}$ ). The  $\lambda_{RF}$  and  $u_{SR}$  terms are based upon observations with a specified exponential profile dependent on  $\cos(\text{latitude})$  which is empirically found to best match PVO and VEX observations. The realized  $u_{SR}$  profile near the equator is shown in Figure 8c. The resulting  $F_{\text{drag}}$  term is then added to the momentum equation.

[37] Gravity wave drag formulations have been used to simulate possible activity in Venus' atmosphere [Zhang et al., 1996]; new gravity wave parameters derived from VEX observations will help constrain these formulations [e.g., Markiewicz et al., 2007; Sánchez-Lavega et al., 2008; García et al., 2009]. For more detail on the Rayleigh friction and gravity wave drag formulations, see Bougher et al. [1988].

[38] The eddy diffusion coefficient is prescribed in the form  $K = A/\sqrt{n}$  with units of  $\text{cm}^2 \text{ s}^{-1}$ , where  $n$  is the total number density and  $A$  is a constant estimated to be  $5.5 \times 10^{12}$  for the nightside [von Zahn et al., 1979]. The nightside eddy diffusion has a maximum of  $1 \times 10^7 \text{ cm}^2 \text{ s}^{-1}$  and the dayside has a constant value for the entire upper atmosphere of  $1 \times 10^6 \text{ cm}^2 \text{ s}^{-1}$ . The nightside eddy diffusion profile is represented as the “best case” profile in Figure 15. The eddy diffusion coefficient utilized is smaller than used previously in 1-D models due to the expanded role of mixing by the

VTGCM global wind system [e.g., von Zahn et al., 1979; Stewart et al., 1980; Gérard et al., 1981; Massie et al., 1983; Drossart et al., 2007; Gérard et al., 2008b]. The incorporation of different dayside and nightside eddy diffusion profiles is based upon PVO density observations; i.e., the nightside densities are observed to vary  $\pm 50\%$  which was found to be approximately three times more than on the dayside [Keating et al., 1980, 1985; Kasprzak et al., 1988, 1993]. Currently in the VTGCM, the dayside eddy diffusion profile is used from  $\text{SZA} = 0^\circ\text{--}105^\circ$  and the nightside eddy diffusion profile is used from  $\text{SZA} = 106^\circ\text{--}180^\circ$ .

[39] The associated boundary conditions are as follows. The top boundary assumes  $dT/dz = 0$ ,  $du/dz = dv/dz = dw/dz = 0$  and the composition is in diffusive equilibrium, thus  $L\Psi = 0$ . The bottom boundary presently assumes all winds are zero and a temperature value of 230 K is prescribed. A return flow (night to day) is neglected, thus  $\Psi_O = 1.2 \times 10^{-10}$  [Yung and Demore, 1982] and  $\Psi_{CO} = 5.8 \times 10^{-5}$  (where  $\Psi$  is mass mixing ratio) and  $N_2$  is calculated as a simple diffusive equilibrium constituent above  $z_p = 0$  (the homopause). The O boundary condition does not allow O escape due to the presence of the low altitude trace species, which shorten the O lifetime dramatically when compared to the eddy diffusion timescale near 80 km. The mass mixing ratio for CO<sub>2</sub> is derived by  $\Psi_{CO_2} = 1.0 - \Psi_{CO} - \Psi_O - \Psi_{N_2}$ . The minorspecies lower boundary values are set according to global averaged values given by Yung and Demore [1982] and the ions are in photochemical equilibrium. The leapfrog scheme is chosen for the temporal discretization.

[40] The most recent VTGCM model changes are crucial to properly reproduce VEX observations. The VTGCM lower boundary is now extended downward and the upper boundary is extended upward. The altitude range at local noon currently spans ~70 km to 300 km. This insures that all the dynamical influences contributing to the NO UV and O<sub>2</sub> IR nightglow layers can be captured. “Exact” (line-by-line radiative transfer model) CO<sub>2</sub> 15  $\mu\text{m}$  cooling rates for a given temperature and composition profile are taken from Roldán et al. [2000]; cooling rates for the simulated VTGCM temperatures and species abundances are calculated (from these “exact” rates) based upon a slight modification of the parameterization scheme described previously [e.g., Bougher et al., 1986]. The near-IR heating term is incorporated using offline simulated look-up tables, updated recently using Roldán et al.'s [2000] rates. Roldán et al. [2000] discusses the detailed NLTE radiative transfer model, which “computes the populations of more than 60 vibrational levels of the four major isotopes of CO<sub>2</sub>, and the cooling and heating rates by more than 90 radiative transitions”. Further discussion by Roldán et al. [2000] compares their results with previous calculations [e.g., Dickinson, 1972; Deming and Mumma, 1983; Gordiets and Panchenko, 1983; Stepanova and Shved, 1985; Dickinson and Bougher, 1986] and explains the improvements in the heating and cooling rates. The most noticeable improvement from adding the new IR heating rates into the VTGCM is found in the doubling of the 4.3  $\mu\text{m}$  heating around 120 km on the dayside.

### 2.2.2. NO UV Nightglow and N Production

[41] The NO UV nightglow emission and N atom production have been updated with the application of solar

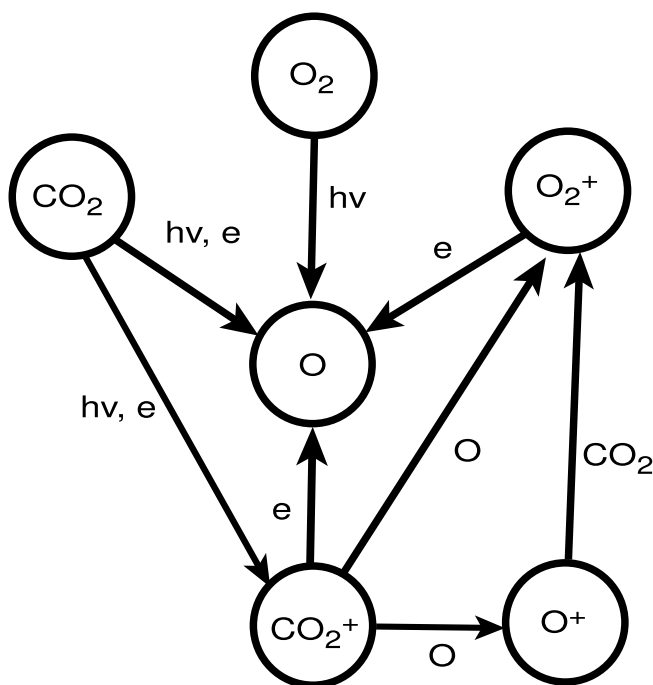


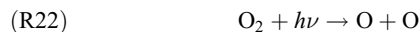
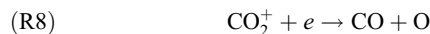
**Figure 2.** VTGCM simplified dayside odd oxygen chemical scheme. This provides the sources for atomic O which is transported to the nightside to produce the O<sub>2</sub> IR and NO UV night airglow emissions.

photodissociation and photoelectron dissociation rates of N<sub>2</sub> for solar minimum or maximum conditions, based upon detailed 1-D model simulations by J.-C. Gérard [e.g., Gérard *et al.*, 2008a]. In these calculations, the cross sections for the N<sub>2</sub> dissociation by solar UV photons are obtained as the difference between the total absorption and the ionization cross sections. High resolution cross sections and predissociation probabilities are needed to quantitatively model the production of atomic nitrogen. Fox *et al.* [2008] have stated this to be important for the highly structured regions of the N<sub>2</sub> photoabsorption spectrum shortward of the ionization threshold at 79.6 nm where predissociation and autoionization compete. Currently high resolution cross sections are being measured and predissociation lifetimes are being calculated. Even with this progress there is still insufficient information (e. g. branching ratios) to compute the production rates of atomic nitrogen or the total photodissociation rate of N<sub>2</sub> [Fox *et al.*, 2008]. Instead, the use of lower resolution solar fluxes and cross sections can provide accuracy to a “factor of only a few” [Fox *et al.*, 2008]. More accurate rates are presently approximated within the VTGCM by tripling the rates calculated for large wavelength bins (low resolution). These new N production rates provide proper chemical sources of atomic nitrogen on the dayside coupled with transport to the nightside to produce the NO UV night airglow.

### 2.2.3. Updated Airglow Chemistry

[42] Another VTGCM modification involves updates of the night airglow chemistry with recent reaction rates and yields. Illustrated in Figure 2 are sources and sinks for atomic oxygen on the dayside. The selected reactions are

listed in order of decreasing importance for atomic oxygen production:



There are two altitude regions where O is produced. The production peaks for reactions (R21) and (R22) are near 110 km, while reactions (R7) and (R8) peak near 140 km. The two different altitude source regions are important for the production of the O<sub>2</sub> IR night airglow and the NO UV nightglow, respectively.

[43] Figure 3 illustrates the chemical processes, sources and sinks, controlling the dayside atomic nitrogen abundance [Bougher *et al.*, 1990]. The main sources of atomic nitrogen come from photodissociation and photoelectron impact of molecular nitrogen (see section 2.2.2). These reactions can supply both ground state and excited atomic nitrogen, N(<sup>4</sup>S) and N(<sup>2</sup>D), respectively. The branching ratio used for N(<sup>2</sup>D) is  $f = 0.5$  [Bougher *et al.*, 1990]. There are four selected reactions that regulate dayside atomic nitrogen,

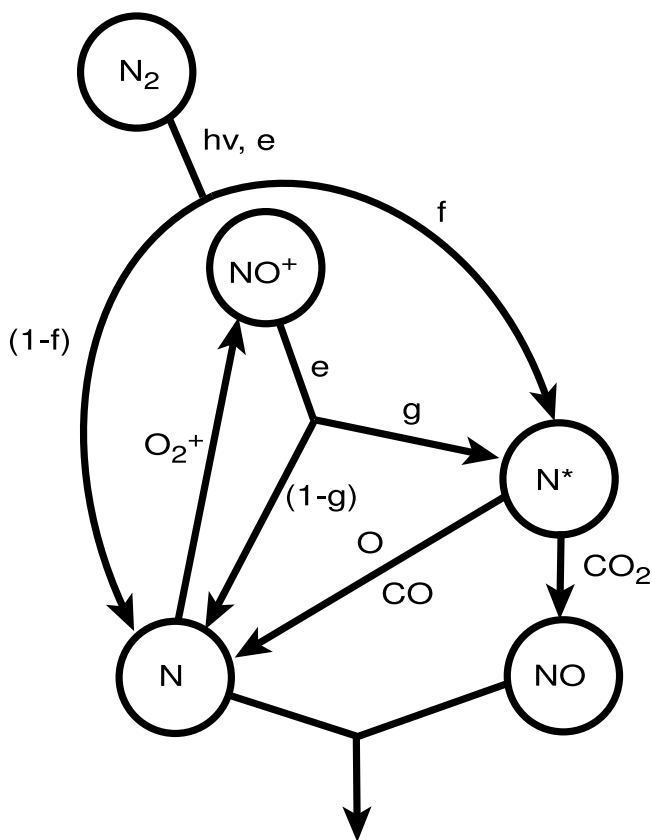


**Figure 3.** VTGCM simplified dayside odd nitrogen chemical scheme. Taken from Bougher *et al.* [1990].

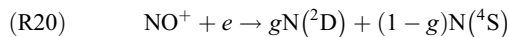
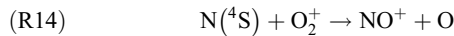
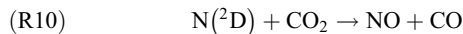


**Table 1.** Key O<sub>2</sub> IR and NO UV Nightglow Parameters<sup>a</sup>

	Reaction	Value	Source
	O + O + CO <sub>2</sub> → O <sub>2</sub> (a state)	75% yield	<i>Gérard et al.</i> [2008b]
(R1)	O + O + CO <sub>2</sub> → O <sub>2</sub> (a state)	$2.75 \times 10^{-32}$	<i>Campbell and Gray</i> [1973]
(R2)	O <sub>2</sub> (a state) + CO <sub>2</sub> → O <sub>2</sub> + CO <sub>2</sub>	$2 \times 10^{-20}$	<i>Sander et al.</i> [2003]
(R3)	O + CO + CO <sub>2</sub> → 2CO <sub>2</sub>	$6.5 \times 10^{-33} \times \exp(-2180/T_n)$	<i>Baulch et al.</i> [1980]
(R4)	O + O <sub>2</sub> + CO <sub>2</sub> → O <sub>3</sub> + CO <sub>2</sub>	$1.35 \times 10^{-33}$	<i>Hampson</i> [1980]
(R5)	CO <sub>2</sub> <sup>+</sup> + O → O <sup>+</sup> + CO <sub>2</sub>	$9.60 \times 10^{-11}$	<i>Fox and Sung</i> [2001]
(R6)	CO <sub>2</sub> <sup>+</sup> + O → O <sub>2</sub> <sup>+</sup> + CO	$1.64 \times 10^{-10}$	<i>Fehsenfeld et al.</i> [1970]
(R7)	O <sub>2</sub> <sup>+</sup> + e → O + O	$1.95 \times 10^{-7} \times (300/T_e)^{0.7}$	<i>Mehr and Biondi</i> [1969]
(R8)	CO <sub>2</sub> <sup>+</sup> + e → CO + O	$3.5 \times 10^{-7} \times (300/T_e)^{0.5}$	<i>Gougousi</i> [1997]
(R9)	O <sup>+</sup> + CO <sub>2</sub> → O <sub>2</sub> <sup>+</sup> + CO	$1.10 \times 10^{-09}$	<i>Anicich</i> [1993]
	f	0.5 branching ratio	<i>Bougher et al.</i> [1990]
	g	0.75 branching ratio	<i>Bougher et al.</i> [1990]
(R10)	N( <sup>2</sup> D) + CO <sub>2</sub> → NO + CO	$2.8 \times 10^{-13}$	<i>Bougher et al.</i> [1990]
(R11)	N( <sup>2</sup> D) + O → N( <sup>4</sup> S) + O	$2.0 \times 10^{-11}$	<i>Bougher et al.</i> [1990]
(R12)	N( <sup>2</sup> D) + CO → N( <sup>4</sup> S) + CO	$1.9 \times 10^{-12}$	<i>Herron</i> [1999]
(R13)	N( <sup>2</sup> D) + N <sub>2</sub> → N( <sup>4</sup> S) + N <sub>2</sub>	$1.7 \times 10^{-14}$	<i>Herron</i> [1999]
(R14)	N( <sup>4</sup> S) + O <sub>2</sub> <sup>+</sup> → NO <sup>+</sup> + O	$1.00 \times 10^{-10}$	<i>Scott et al.</i> [1998]
(R15)	N( <sup>4</sup> S) + NO → N <sub>2</sub> + O	$2.5 \times 10^{-10} (T_n/300)^{0.5} \exp(-600/T_n)$	<i>Fox</i> [1994]
(R16)	N( <sup>4</sup> S) + O → NO* + hν	$1.9 \times 10^{-17} (300/T_n)^{0.5} (1 - 0.57/T_n^{0.5})$	<i>Dalgarno et al.</i> [1992]
(R17)	N( <sup>4</sup> S) + O + CO <sub>2</sub> → NO + CO <sub>2</sub>	$1.83 \times 10^{-32} (298/T_n)^{0.5}$	<i>Campbell and Thrush</i> [1966]
(R18)	N <sub>2</sub> + O <sup>+</sup> → NO <sup>+</sup> + N	$1.2 \times 10^{-12} (300/T_n)^{0.45}$	<i>Hierl et al.</i> [1997]
(R19)	NO + O <sub>2</sub> <sup>+</sup> → NO <sup>+</sup> + O <sub>2</sub>	$4.50 \times 10^{-10}$	<i>Midey and Viggiano</i> [1999]
(R20)	NO <sup>+</sup> + e → gN( <sup>2</sup> D) + (1-g)N( <sup>4</sup> S)	$4.0 \times 10^{-7} (300/T_e)^{0.5}$	<i>Vejby-Christensen et al.</i> [1998]
(R21)	CO <sub>2</sub> + hν → CO + O		computed in the VTGCM
(R22)	O <sub>2</sub> + hν → O + O		computed in the VTGCM
(R23)	N <sub>2</sub> + hν → (1-f)N( <sup>4</sup> S) + fN( <sup>2</sup> D)		computed in the VTGCM

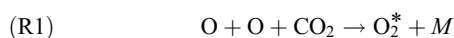
<sup>a</sup>Rate coefficients are cm<sup>3</sup> s<sup>-1</sup>, and three body rate coefficients are cm<sup>6</sup> s<sup>-1</sup>

plus N(<sup>2</sup>D) quenching by atomic oxygen and carbon monoxide:



The dissociative recombination of NO<sup>+</sup> also supplies ground state and excited atomic nitrogen species; thus a branching ratio of  $g = 0.75$  is used for N(<sup>2</sup>D) [*Bougher et al.*, 1990]. The dayside atomic nitrogen production peak is located near the ionospheric peak at 140 km.

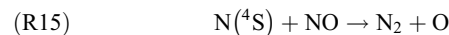
[44] The two dayside produced atomic species, nitrogen and oxygen, are subject to transport by the global thermospheric circulation. Upwelling occurs on the dayside with strong cross terminator horizontal flow and downwelling on the nightside. These species follow the global circulation streamlines to the nightside at different altitudes. The streamlines closely follow constant pressure surfaces. Therefore, the streamlines decrease in altitude from day to night due to the colder nightside temperatures and downwelling of the converging global circulation. The main chemical reaction for O<sub>2</sub> IR night airglow production and the main chemical loss of atomic oxygen on the nightside (above ~90 km) is



The O<sub>2</sub> IR emission is assumed to be optically thin and uses a typical yield of 75% [e.g., *Gérard et al.*, 2008b] for the O<sub>2</sub> IR production. There are other estimated yields, such as that of *Crisp et al.* [1996], which are based on laboratory studies. They found yields of  $0.63 \pm 0.19$  for  $M = N_2$  and  $\sim 0.6\text{--}0.75$  for  $M = CO_2$ . Another estimated yield was presented by *Huestis* [2002]; values of 0.94–0.99 were generated for  $M = N_2$  and  $M = CO_2$  by combining laboratory studies and atmospheric studies. The formulation for the O<sub>2</sub> (<sup>1</sup>Δ) 1.27 μm emission is retained from *Bougher and Borucki* [1994]. The main chemical loss on the nightside for N(<sup>4</sup>S) and the main chemical reaction for production of the NO UV night airglow is



Reaction (R16) provides emissions for both delta and gamma bands. For the NO UV emission it is assumed to be optically thin and utilizes a yield of 100%. See *Bougher et al.* [1990] for more details. This reaction competes strongly with



For a summary of all the reactions, reaction rates, and yields used within the VTGCM for atomic oxygen and atomic nitrogen see Table 1.

### 2.3. Reevaluated Chemical Rate Coefficients

[45] In this section, two reaction rates are discussed, (R1) (O + O + M) and (R17) (N + O + M). Preliminary laboratory measurements and evaluations of these rates are currently available, resulting in updated rates for use in the new VTGCM simulations (see Table 2).

**Table 2.** Key Chemical Reaction Rate Tests (cm<sup>6</sup> s<sup>-1</sup>)

	(R1) (O + O + M)	(R17) (N + O + M)
Standard	$2.75 \times 10^{-32}$ [Campbell and Gray, 1973]	$1.83 \times 10^{-32} (298/T_n)^{0.5}$ [Campbell and Thrush, 1966]
Test	$1.8 \times 10^{-32}$ [Jamieson et al., 2009b]	$1.1 \times 10^{-32} (300/T_n)^{0.5}$ [Stewart and Barth, 1979]

[46] Research previously published in the literature uses the rate constant of (R1) =  $2.75 \times 10^{-32}$  cm<sup>6</sup> s<sup>-1</sup> [Gérard et al., 2008c; Nair et al., 1994; Campbell and Gray, 1973] for Venus and Mars where CO<sub>2</sub> is the background atmosphere. However, this rate constant has only been properly evaluated for the case of the Earth, which has a background atmosphere of N<sub>2</sub>, based on the work by Campbell and Gray [1973]. This rate for M = N<sub>2</sub> is then multiplied by a factor of 2.5 [Nair et al., 1994] for an estimation of the relative efficiency of CO<sub>2</sub> (versus N<sub>2</sub>) as the third body. The 2.5 factor is very weakly supported and documented. Nair et al. [1994] provide no numerical details about how they derived their factor of 2.5 (D. L. Huestis, private communication, 2010). Recently, a preliminary rate coefficient has been measured and suggested for a predominantly CO<sub>2</sub> background atmosphere [Jamieson et al., 2009a, 2009b; D. L. Huestis, private communication, 2010]. This preliminary rate, (R1) =  $1.8 \times 10^{-32}$  cm<sup>6</sup> s<sup>-1</sup> at 200 K, is slower than what has been used in the past. This implies that three-body recombination should occur at a lower altitude (higher CO<sub>2</sub> density) in the Venus atmosphere, with a corresponding lowered O<sub>2</sub> nightglow layer as well. A sensitivity test has been completed using the preliminary (test) rate in the VTGCM and the model results are discussed in section 3.3.3.

[47] The other rate recently revisited is (R17) (see Table 2). In previous VTGCM simulations [Bougher et al., 1990] a rate of  $1.1 \times 10^{-32} (300/T_n)^{0.5}$  cm<sup>6</sup> s<sup>-1</sup> was used from Stewart and Barth [1979]. Upon closer inspection, the Stewart and Barth [1979] rate is based upon measurements conducted by Baulch et al. [1973], where M = N<sub>2</sub>. As stated above, CO<sub>2</sub> is a more efficient third body than N<sub>2</sub>. Previous measurements were also conducted with a CO<sub>2</sub> background for two different temperatures [Campbell and Thrush, 1966]. One measurement for 196 K gave a rate of  $2.26 \times 10^{-32}$  cm<sup>6</sup> s<sup>-1</sup> and the other for 298 K gave a rate of  $1.83 \times 10^{-32}$  cm<sup>6</sup> s<sup>-1</sup>. For our new VTGCM, a temperature dependent rate was derived using these two measurements, giving a rate of  $1.83 \times 10^{-32} (298/T_n)^{0.5}$  cm<sup>6</sup> s<sup>-1</sup>, where  $T_n$  is the neutral temperature. The change in this rate does not impact the O<sub>2</sub> IR nightglow but slightly changes the NO UV nightglow. See section 3.3.3 for the VTGCM model results and section 4.2 for comparisons to available observations.

#### 2.4. Chemical Trace Species at Lower Altitudes

[48] A final chemical update to the VTGCM is implemented by adding nightside profiles of specific chemical trace species. Krasnopolsky's [2010] calculations suggest that other odd O loss processes may be important on the nightside involving trace species that impact nightglow emissions [Krasnopolsky, 2010]. Trace species have been added to the VTGCM before, but the profiles used were diurnally averaged [Bougher and Borucki, 1994; Yung and Demore, 1982]. At that time, trace species did make a notable difference in

the O density profiles at low thermospheric altitudes [see Bougher and Borucki, 1994, Figure 8].

[49] Currently, single density profiles of trace species (Cl, Cl<sub>2</sub>, ClCO, ClO, H<sub>2</sub>, HCl, HO<sub>2</sub>, O<sub>3</sub>, OH) from an altitude of ~70 km to 130 km for the nightside have been extracted from Krasnopolsky [2010, Figure 8] and incorporated into the nightside of the VTGCM. Krasnopolsky [2010] employs a 1-D photochemical model that is tuned for nightside conditions (photolysis is not involved) which includes 61 reactions and 24 species. As stated by Krasnopolsky [2010], the model results are within observational ranges for the O<sub>2</sub> IR, NO UV, and OH IR nightglow emissions and peak altitudes. Therefore, VTGCM reaction rates involving these trace species are taken from Krasnopolsky [2010, Table 4] with additional reaction rates from Yung and Demore [1982].

[50] It is appropriate not to carry these trace species dynamically in the VTGCM. This is justified because in the region where the trace species greatly impact the atmospheric chemistry, they have very short chemical lifetimes with respect to the dynamics. When these trace species were added to the VTGCM, they made a noticeable difference in the nightglow layers (see section 3.3.4). They provide additional loss terms for the O chemistry at the lower altitudes (below 90 km) and help define a narrower O density layer. This directly impacts the O<sub>2</sub> IR nightglow and indirectly impacts the NO UV nightglow. Without these trace species, the chemistry is incomplete in the VTGCM and the varying nightglow emission layers cannot be properly simulated for comparison to available data sets.

### 3. VTGCM Simulation Results

[51] This section outlines the inputs specified for a VTGCM best case (also referred to as a “mean” simulation) and illustrates specific results for the Venus upper atmosphere structure and dynamics (e.g., temperatures, winds, O and N(<sup>4</sup>S) densities, O<sub>2</sub> IR and NO UV nightglow emissions). A “mean” simulation is computed using static input parameters (section 3.1) and boundary conditions (section 2.2), and the model is run to a steady state solution. Steady state is determined by the difference between the last simulated model day and the previous simulated model day having a percent difference of less than 2% for all prognostic fields. For the VTGCM, a typical simulation takes about 9 simulated Earth days to reach such a steady state condition starting from a symmetric wind condition. Once a realistic “mean” simulation is completed, sensitivity tests are performed with two adjustable parameters (maximum nightside eddy diffusion and wave drag impacting the global wind system). In addition, an evaluation is made of the chemical impacts by varying key reaction rates and adding chemical trace species. The purpose of this section is to examine the VTGCM “mean” simulation results using VEX parameters and to demonstrate the VTGCM sensitivity to specific input parameters. Data-model comparison is conducted in section 4, specifically focused on VEX measurements.

#### 3.1. “Mean” Simulation: Parameters for VEX Conditions

[52] In order to simulate mean conditions for the Venus' middle and upper atmospheres during VEX sampling periods, the VTGCM is run with solar minimum fluxes (F10.7 = 70

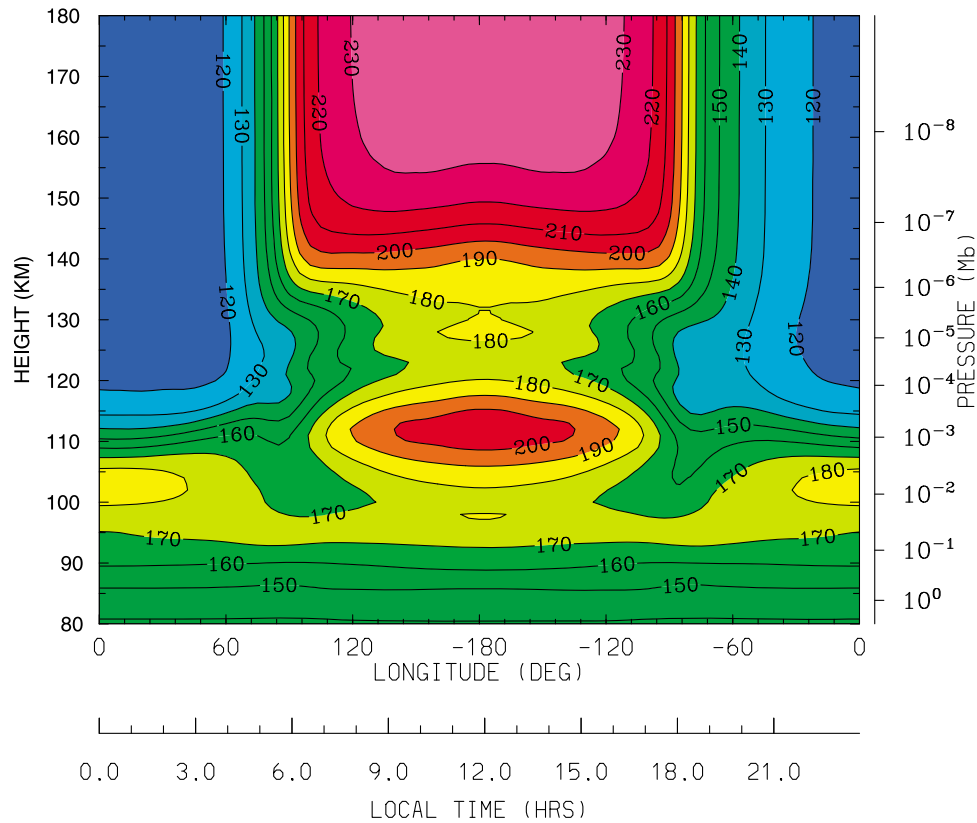


**Figure 4.** VTGCM “mean” case for VEX conditions; longitude-height cross section at 2.5°N (local time versus height) for temperature (K).

at 1 AU), a nightside maximum eddy diffusion of  $1.0 \times 10^7 \text{ cm}^2 \text{ s}^{-1}$  and a wave drag parameter ( $\lambda_{RF}$ ) of  $0.5 \times 10^{-4} \text{ s}^{-1}$ . Mean VEX conditions are best captured by VEX statistically averaged mean nightglow emission maps. Presently, the O<sub>2</sub> IR statistical map (observed emissions averaged spatially and temporally) exists and is used for data-model comparisons for mean conditions [Gérard *et al.*, 2008b; Piccioni *et al.*, 2009; Soret *et al.*, 2011]. Other maps have been created for single orbits and are being used to observe the nightglow morphology [Hueso *et al.*, 2008]. The NO UV statistical map is being developed and has provided initial information on the averaged nightglow morphology [Cox, 2010].

### 3.2. “Mean” Simulation: Results

[53] The measured thermal structure of Venus’ upper atmosphere has several interesting characteristics that the VTGCM reproduces in its “mean” simulation. Figure 4 represents the simulated thermal structure near the equator at 2.5°N. At the exobase ( $\sim 190 \text{ km}$ ), temperatures range from 238 K on the dayside to 114 K on the nightside. At 12:00 LT near 112 km is a warm region, about 207 K, created by near IR (i.e., mostly  $4.3 \mu\text{m}$ ) heating. Near 00:00 LT, a warm region is produced at 103 km with a simulated temperature around 188 K. Figure 5 illustrates the heating and cooling rates at 12:00 LT and 00:00 LT. On the dayside, there is mostly a radiative balance with small influences from

dynamics. However, on the nightside the temperatures are regulated by the magnitude of dynamical terms.

[54] Figure 6a shows a 1D representation of the nightside temperature profile. The nightside warm region is associated with the dayside warm region (in the lower thermosphere) and the resulting day-to-night global circulation, which produces dynamical heating near midnight. The total dynamical heating rate (adiabatic + total (horizontal + vertical) advection) at 103 km near the antisolar point is  $64 \text{ K d}^{-1}$  (see Figure 6b). This heating rate is dominated by adiabatic heating at 103 km near midnight. Above 130 km on the nightside, temperatures remain cold at 114 K. Thus the new VTGCM simultaneously reproduces the nightside cryosphere ( $>130 \text{ km}$ ) characterized by PVO observations and reproduced by previous modeling efforts [Keating *et al.*, 1979; Bougher *et al.*, 1997], and the observed warm nightside temperature near 100 km at midnight (see section 4.1).

[55] The neutral zonal winds near the equator are illustrated in Figure 7. The evening terminator (ET) winds are  $143 \text{ m s}^{-1}$  at  $\sim 110 \text{ km}$ ,  $202 \text{ m s}^{-1}$  at  $\sim 120 \text{ km}$ , and reach a maximum at  $314 \text{ m s}^{-1}$  near 180 km. The morning terminator (MT) winds are  $-135 \text{ m s}^{-1}$  near 110 km,  $-130 \text{ m s}^{-1}$  near 120 km, and are maximum at  $-191 \text{ m s}^{-1}$  near 172 km. The ET winds are faster than the MT winds since the drag term is prescribed asymmetrically in local time in order to mimic the observed upper atmosphere RSZ winds (see Figure 8c). It is noteworthy that the VTGCM captures the shift in the convergence of the flow away from midnight and

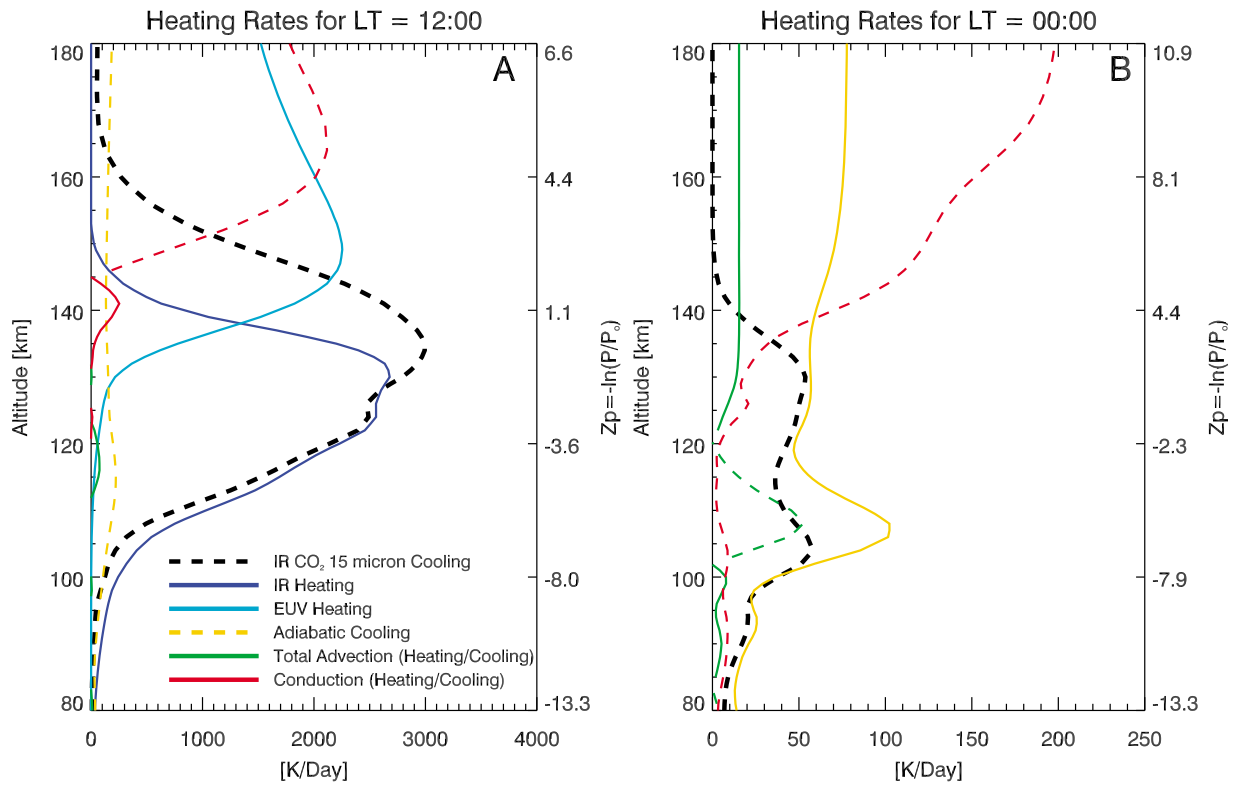


**Figure 5.** The heating and cooling terms at (a) 12:00 LT and (b) 24:00 LT near the equator. The dashed lines represent cooling, and the solid lines represent heating.

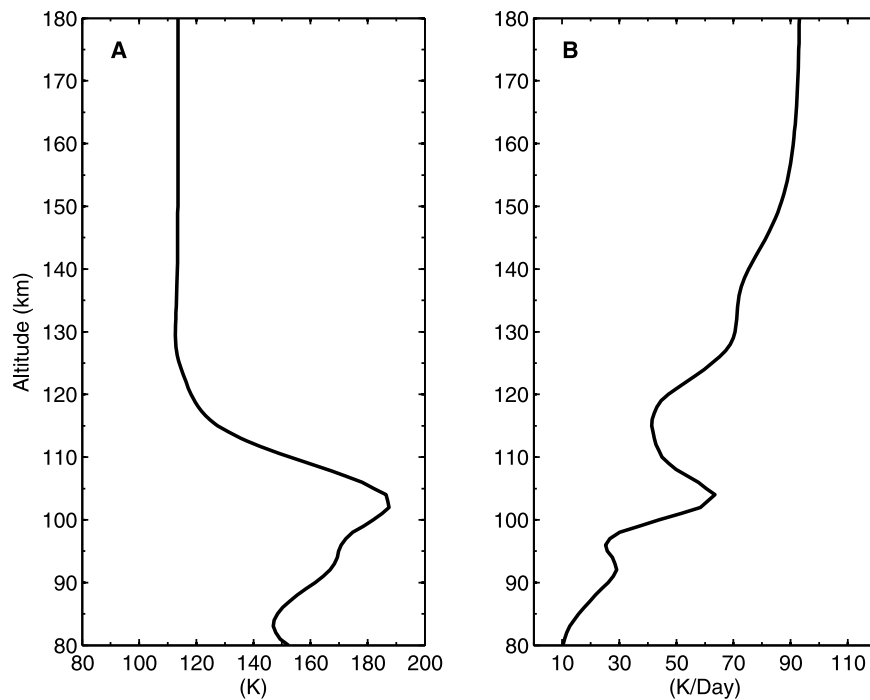


**Figure 6.** VTGCM “mean” case profiles at 2.5°N: (a) temperature (K) at 00:00 LT and (b) total dynamical heating rate (K d<sup>-1</sup>) (adiabatic plus total advection) at 00:00 LT.

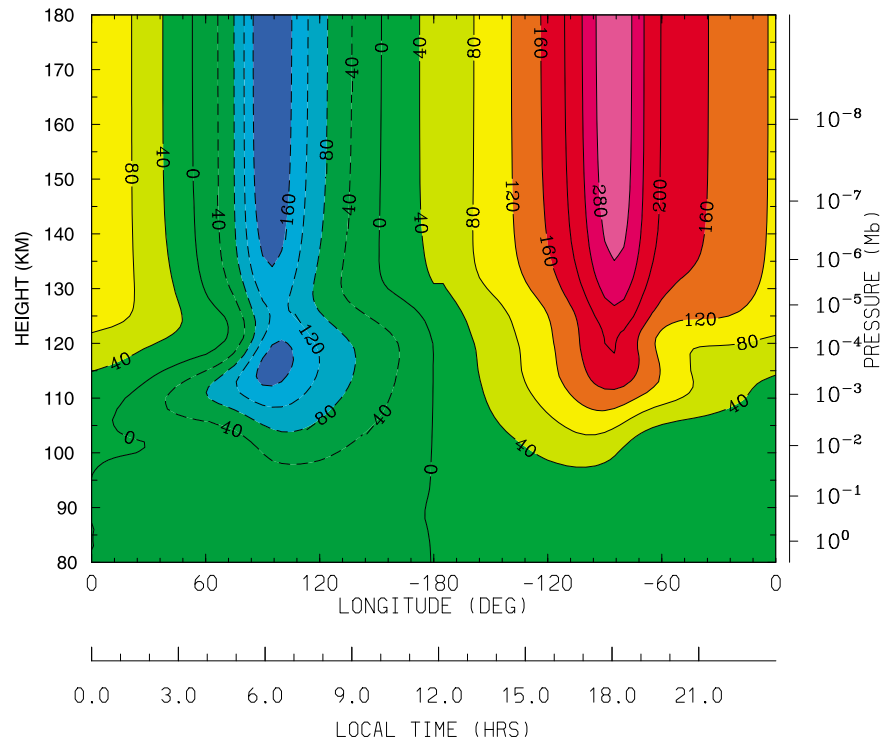


**Figure 7.** VTGCM “mean” case for VEX conditions; longitude–height cross section at 2.5°N (local time versus height) for zonal winds ( $\text{m s}^{-1}$ ).

toward the morning terminator above 110 km. The simulated wind magnitudes are within observed ranges, see the discussion in sections 1.1 and 1.2.3. At this time, it is difficult to make detailed, direct comparisons with wind observations due to the high variability of the wind magnitudes and the geometry used to make these measurements. This VTGCM wind system provides a downward vertical velocity at midnight of  $\sim 0.1 \text{ m s}^{-1}$  at 105 km, which is consistent with other estimates in the literature [Bailey *et al.*, 2008; Ohtsuki *et al.*, 2008] but lower than the Bertaux *et al.* [2007] value of  $0.43 \text{ m s}^{-1}$ .

[56] Figure 8 shows the ET and MT total zonal wind profiles and the prescribed RSZ wind profile near the equator (prescribed using the  $u_{SR}$  term in the wave drag equation). The difference between the terminator symmetric and asymmetric total zonal wind profiles reflects the impact of the prescribed RSZ wind profile (see Figure 8c). The RSZ profile is applied globally with respect to height and  $\cos(\text{latitude})$ , and plays a crucial part in producing the nightglow distributions (i.e., the local time location of the peak emission). In order for the O<sub>2</sub> IR nightglow peak intensity to be produced at midnight, the RSZ needs to be very weak (as shown in Figure 8c), up to  $\sim 110 \text{ km}$ . By contrast, for the NO UV nightglow peak intensity to be positioned near 02:00 LT, the RSZ wind has to be  $30\text{--}60 \text{ m s}^{-1}$ , above  $\sim 110 \text{ km}$ . On the dayside, N(<sup>4</sup>S) atoms are produced near  $\sim 140 \text{ km}$ , and subsequently are transported nightward as they follow descending pressure levels to the colder nightside. The dayside pressure at 140 km is equivalent to the pressure at  $\sim 130 \text{ km}$  on the nightside. For this altitude region, the RSZ wind is  $60 \text{ m s}^{-1}$  which is comparable to estimates from previous measurements [see Bougher *et al.*, 2006, Table 1].

Conversely, O is produced near 110 km on the dayside and descends more gradually to the nightside along constant pressure surfaces owing to a weaker diurnal variation in temperatures in this region. For more details about the impacts RSZ winds have on the nightglow, see sections 4.2 and 4.3.

[57] Another result that contributes to the validation of the chosen eddy diffusion coefficient profiles (day versus night) is shown in Figure 9. Mixing ratios from the VTGCM “mean” case (shown in black) are compared to the VTS3 empirical model values (in red) [Hedin *et al.*, 1983]. The VTS3 model is based upon PVO neutral mass spectrometer in situ measurements (mainly solar maximum conditions) obtained at low latitudes above  $\sim 140 \text{ km}$  and uses the hydrostatic equilibrium assumption to extrapolate mixing ratios below  $\sim 140 \text{ km}$ . Figure 9 (top) illustrates mixing ratios for O, CO, and CO<sub>2</sub> at 12:00 LT. Near the top of the dayside panel, the mixing ratios deviate since the VTGCM currently does not include He, which becomes dominant above  $\sim 195 \text{ km}$  in the VTS3. Otherwise the two models are in favorable agreement. Figure 9 (bottom) expresses mixing ratios for O, CO, CO<sub>2</sub> at 00:00 LT. The calculated mixing ratio peak altitudes and magnitudes match VTS3 values reasonably well. However, there are discrepancies near the bottom of the nightside panel. The VTS3 does not incorporate day to night transport of atomic O and trace species. In this region the VTS3 is strictly an extrapolation from higher altitudes and is used as a first order representation of the thermosphere.

[58] Figure 10 illustrates the atomic oxygen density profiles for noon and midnight near the equator with respect to log pressures (Figure 10, left) and altitude (Figure 10, right).

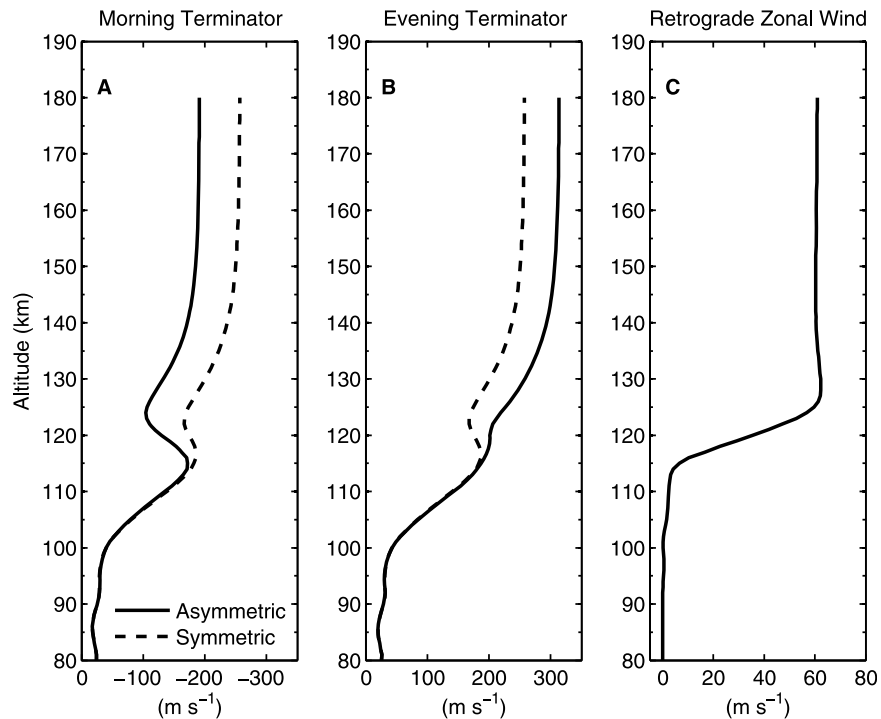


**Figure 8.** VTGCM “mean” case for VEX conditions; longitude-height cross section at 2.5°N: (a) the morning terminator (MT) (06:00 LT) total zonal winds ( $\text{m s}^{-1}$ ) where the solid line represents the asymmetric case, and the dashed line represents the symmetric case, (b) the evening terminator (ET) (18:00 LT) total zonal winds ( $\text{m s}^{-1}$ ) where the solid line represents the asymmetric case and the dashed line represents the symmetric case, and (c) the retrograde zonal winds (RSZ) prescribed as a function with height ( $\text{m s}^{-1}$ ).

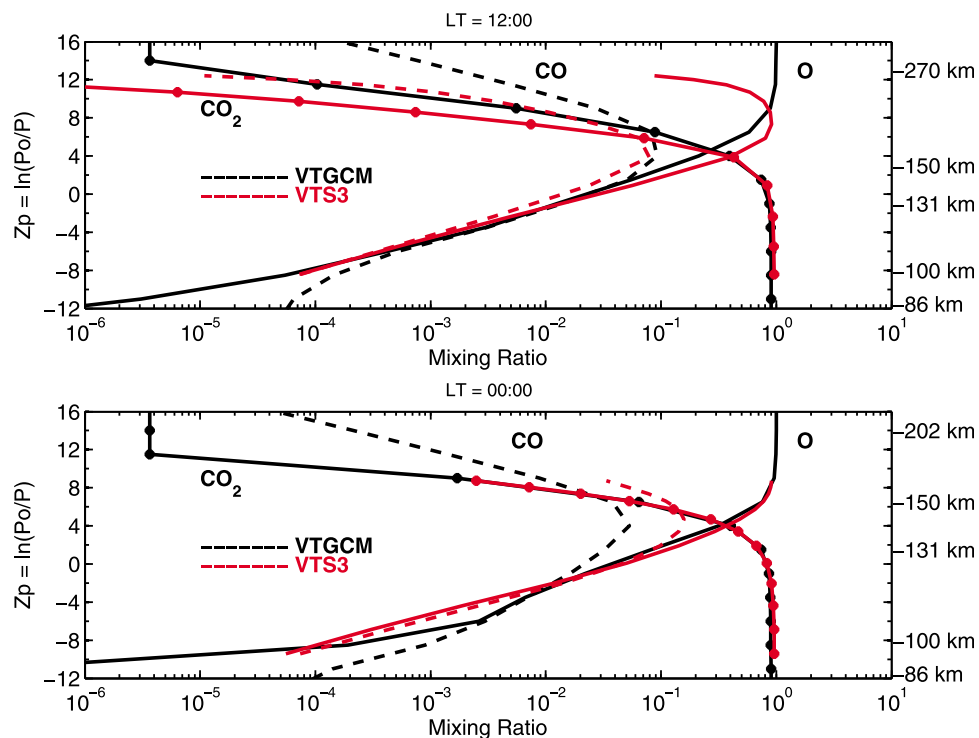


**Figure 9.** VTGCM “mean” case for VEX conditions; mixing ratio profiles at 2.5°N (density versus log pressure and height) represented in black and the empirical VTS3 model is represented in red at (top) 12:00 LT for O, CO, and CO<sub>2</sub> and (bottom) 00:00 LT for O, CO, and CO<sub>2</sub>.

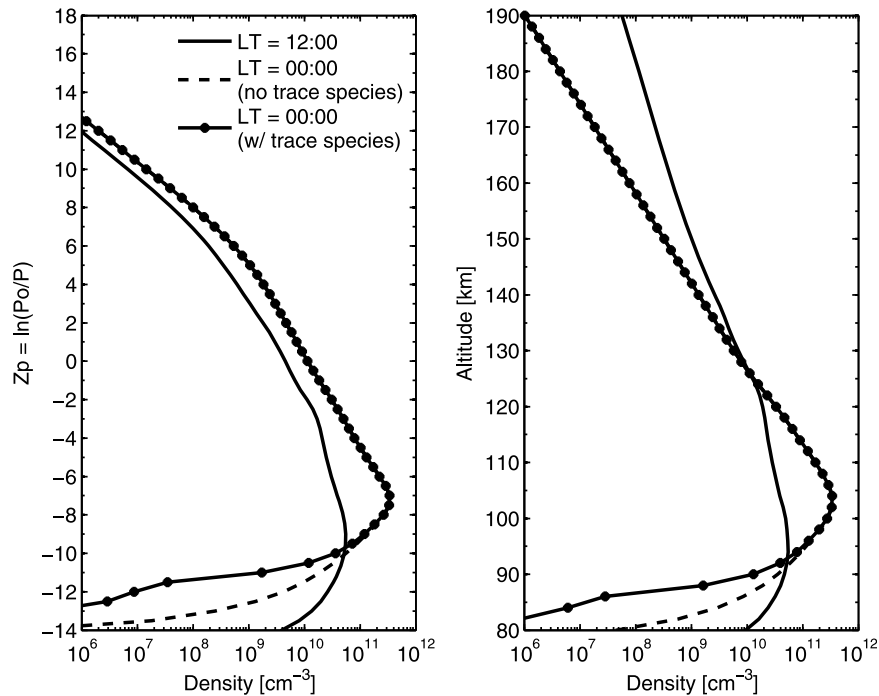


**Figure 10.** VTGCM “mean” case for VEX conditions; density profiles at 2.5°N for atomic oxygen at noon and midnight: (left) density versus log pressure vertical scale; and (right) density versus altitude vertical scale. The density is in units of  $\text{cm}^{-3}$ .

Profiles in Figure 10 (right) are provided from 80 to 190 km to focus on the density structure near the peak. The atomic oxygen density at noon peaks at 94 km with a value of  $5.5 \times 10^{10} \text{ cm}^{-3}$ , while the midnight value is  $3.4 \times 10^{11} \text{ cm}^{-3}$  at 104 km. This ~6 fold enhancement from day to nightside is the result of efficient transport of atomic oxygen atoms from their day side source to their nightside chemical loss at and below 104 km. The VTGCM also produces a noon time O/CO<sub>2</sub> mixing ratio for the dayside at 140 km of 5%. The corresponding net dayside column integrated production (at 60°SZA) for O atoms is calculated to be  $2.34 \times 10^{12} \text{ cm}^{-2} \text{ s}^{-1}$ .

[59] The N(<sup>4</sup>S) density profile for noon and midnight near the equator is shown with respect to log pressure in Figure 11 (left) and with respect to altitude in Figure 11 (right). The altitude plot ranges from 80 km to 190 km to focus on the structure near the density peak. At noon, the peak value near the equator is  $1.0 \times 10^8 \text{ cm}^{-3}$  at 136 km. The nightside density profile peaks at  $1.4 \times 10^8 \text{ cm}^{-3}$  at 115 km near the equator. This 40% fold enhancement, although less pronounced than atomic oxygen, still reflects the combined effects of transport and nightside chemical destruction of atomic nitrogen at and below ~110 km. This is complemented with a net dayside column integrated production at 60°SZA for N(<sup>4</sup>S) of  $1.58 \times 10^{10} \text{ cm}^{-2} \text{ s}^{-1}$ .

[60] The results presented in Figure 12 illustrate the maximum volume emission rate for the O<sub>2</sub> IR nightglow near the equator at ~100 km to be  $1.7 \times 10^6 \text{ (photon cm}^{-3} \text{ s}^{-1})$  with a corresponding peak vertical intensity of 1.76 MR. This peak value is near midnight in concert with the simulated global wind structure. The nightside hemispheric average (defined by a box of 60°S to 60°N and 60°E to 60°W) is ~0.51 MR requiring ~0.22 photons per O atom produced on the dayside and made available to the

nightside for destruction. A 100% yield of the three body reaction ( $\text{O} + \text{O} + \text{CO}_2$ ) for production of O<sub>2</sub> IR nightglow would provide a peak vertical intensity closer to 2.37 MR and a hemispheric average of 0.63 MR.

[61] Figure 13 illustrates the volume emission rate of the NO UV nightglow for the  $\delta$  and  $\gamma$  bands near the equator. The maximum value is  $1.2 \times 10^3 \text{ (photon cm}^{-3} \text{ s}^{-1})$  near 106 km and has a corresponding peak vertical intensity of 1.83 kR. The peak value is shifted toward the morning terminator and is located at ~01:00 LT due to the asymmetrical global winds at 106 km (see Figure 8). The nightside hemispheric intensity average is 0.68 kR. This emission requires 0.04 photons per N atom produced on the dayside and made available to the nightside for destruction. For this “mean” simulation (and incorporating a suite of standard chemical reactions and upgraded rates) the O<sub>2</sub> IR and NO UV night airglow layers are very close in altitude and therefore exist in a relatively similar dynamical region of the upper mesosphere and lower thermosphere.

[62] Timescale plots provide a good measure of the processes which dominate in any given region at a given time. Figure 14 shows vertical profiles of the atomic oxygen and N(<sup>4</sup>S) chemical lifetimes, eddy and molecular diffusion lifetimes, and dynamical (horizontal and vertical winds) lifetimes at 00:00 LT in units of days. The chemical lifetime is calculated as the inverse of loss frequency with atomic oxygen (or N(<sup>4</sup>S)) being the chemical species of concern, since it is the major contributor for the reaction of the O<sub>2</sub> IR (or NO UV) night airglow. Eddy diffusion lifetime is estimated by  $\tau_{\text{eddy}} = H^2/K_{\text{eddy}}$ , where  $H$  is the mean scale height ( $H = RT/mg$ , where  $R$  is universal gas constant,  $T$  is neutral temperature,  $m$  is mean molecular weight,  $g$  is gravity), and  $K_{\text{eddy}}$  is the eddy diffusion coefficient. Above ~130 km  $\tau_{\text{eddy}}$

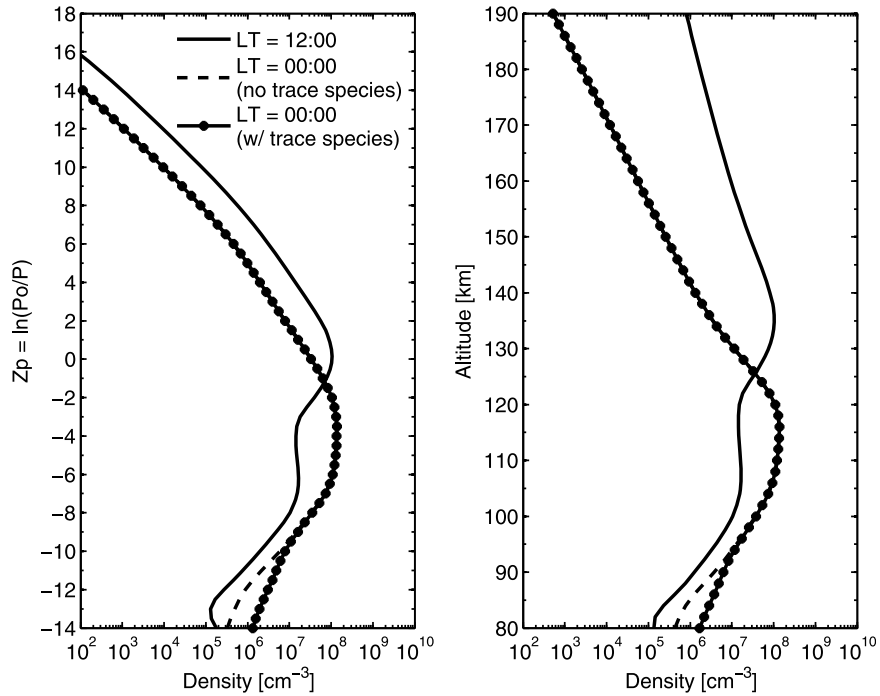


**Figure 11.** VTGCM “mean” case for VEX conditions; density profiles at 2.5°N for N(4S) at noon and midnight: (left) density versus log pressure vertical scale; and (right) density versus altitude vertical scale. The density is in units of cm<sup>-3</sup>.

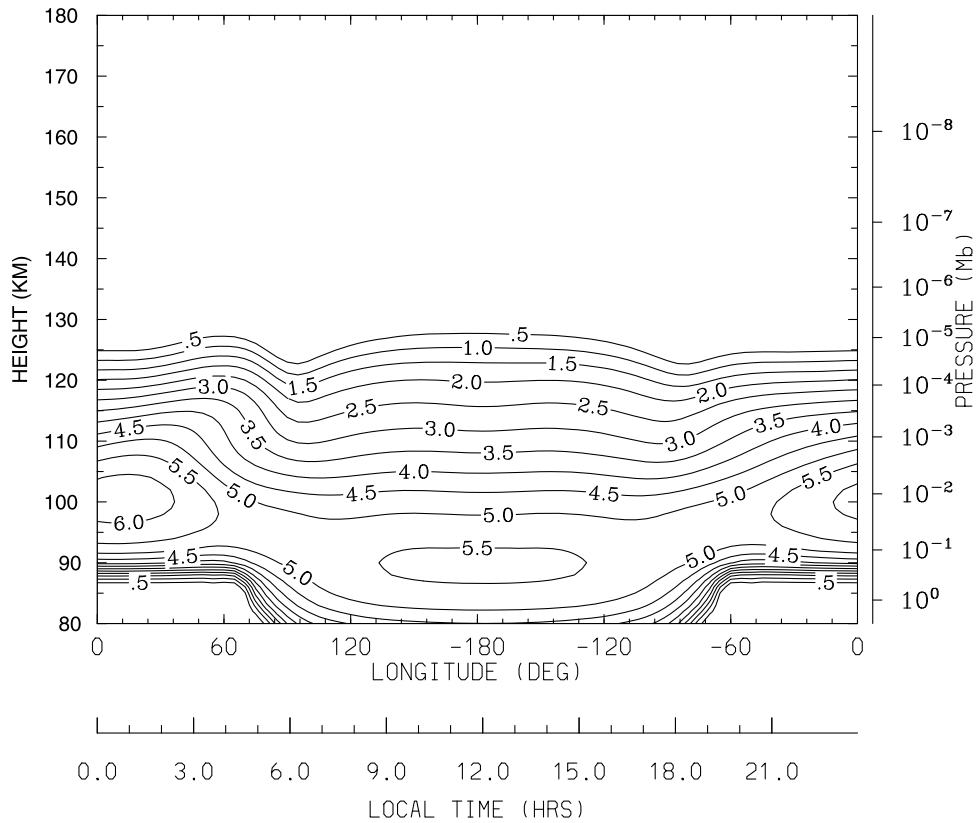


**Figure 12.** VTGCM “mean” case for VEX conditions; longitude-height cross section at 2.5°N (local time versus height) illustrates a maximum O<sub>2</sub> IR night airglow volume emission rate close to midnight. The emission rate unit is log<sub>10</sub> (photons cm<sup>-3</sup> s<sup>-1</sup>).



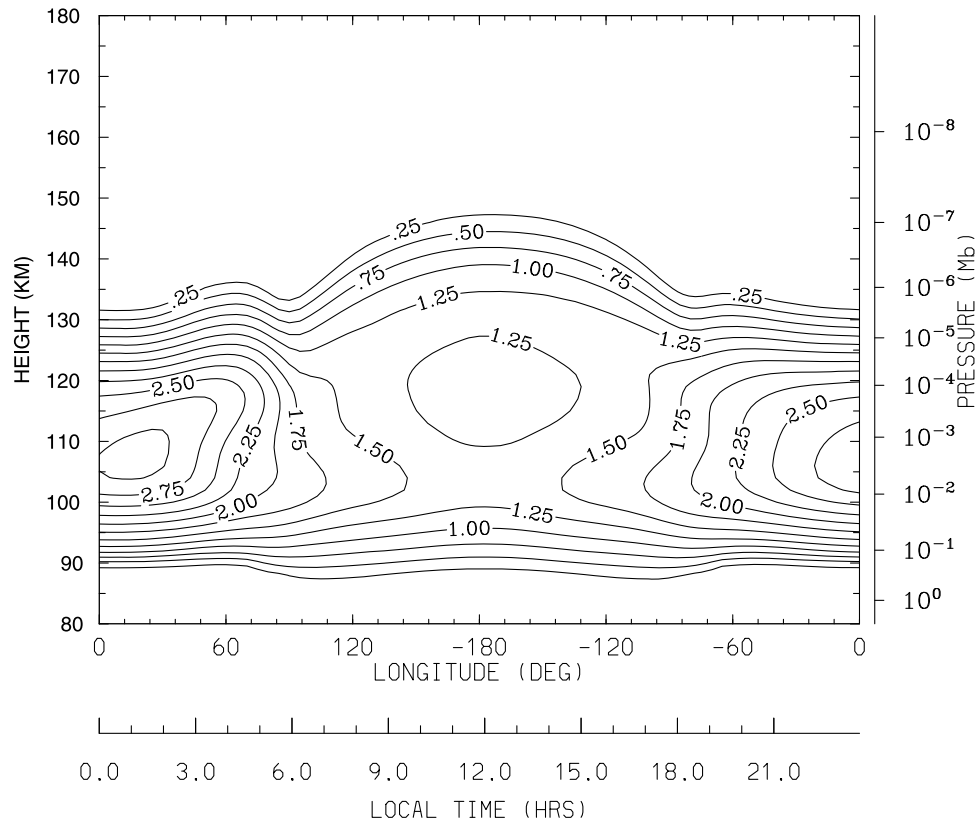


**Figure 13.** VTGCM “mean” case for VEX conditions; longitude-height cross section at 2.5°N (local time versus height) illustrates a maximum NO UV night airglow volume emission rate close to 01:00 LT. The emission rate unit is  $\log_{10}$  (photons  $\text{cm}^{-3} \text{s}^{-1}$ ).

decreases due to  $H$  increasing; this results from the increasing importance of atomic oxygen above  $\sim 130$  km despite nearly constant temperatures. The molecular diffusion lifetime is calculated as  $\tau_D = H^2/D$ , where  $D$  is the molecular diffusion coefficient for O in a CO<sub>2</sub> atmosphere. For more details on the formulation of  $D$ , see Dickinson and Ridley [1972]. The lifetimes of eddy diffusion and molecular diffusion are equal near 127 km, resulting in a homopause at 127 km on the nightside. This homopause location (neglecting the mixing influence of the VTGCM global winds) is  $\sim 4$  km lower than 1-D model predictions of Massie *et al.* [1983], which uses a maximum eddy diffusion of  $5 \times 10^7 \text{ cm}^2 \text{ s}^{-1}$ . The lifetime corresponding to the horizontal wind (motion of a parcel) utilizes the wind velocity on the evening terminator; i.e., it is the location of the fastest horizontal winds and therefore a dominant contributor to the distribution of chemical species. The vertical wind lifetime is  $\tau_{\text{vertical}} = H/w$ , where  $\tau_{\text{vertical}}$  is the vertical velocity lifetime and  $w$  is vertical velocity. Both nightglow emissions are controlled mainly by the strength of the global circulation which transports O and N(<sup>4</sup>S) atoms from the dayside. In the case of the O<sub>2</sub> IR night airglow, the timescale plot reveals the eddy diffusion lifetime matches the O chemical lifetime at 100 km, while dynamics plays a role at higher altitudes. Therefore eddy diffusion is the dominating process in the region where the volume emission rate of the O<sub>2</sub> IR night airglow peaks. For N(<sup>4</sup>S), the altitude of the nightglow is different from O<sub>2</sub> IR night airglow and it is controlled by the vertical

wind lifetime and the N(<sup>4</sup>S) lifetime match at 105 km. Therefore the timescale plot shows the vertical velocity dominating the region where the NO UV nightglow peaks, while the eddy diffusion timescale is not competitive enough to make a significant impact on the nightglow altitude peak. If the winds are slowed down sufficiently to let eddy diffusion dominate, day to night transport of O and N atoms is inadequate to provide the source for the intense emissions of O<sub>2</sub> IR or NO UV nightglow observed.

### 3.3. Sensitivity Tests on the “Mean” Simulation

[63] As mentioned in the introduction (section 1), our purpose for VTGCM analysis of VEX data sets is to understand the processes controlling the variable night airglow layers. The O<sub>2</sub> IR and NO UV night airglow layers were subsequently examined for their sensitivity to two adjustable parameters in the VTGCM model (i.e., the maximum nightside eddy diffusion and the strength of the Rayleigh friction (impacting the global wind system)). A discussion follows about the chemical impacts on the nightglow emissions and their distributions.

#### 3.3.1. Sensitivity Tests: Eddy Diffusion

[64] For the eddy diffusion test, the maximum eddy diffusion coefficient is varied, consistent with the observed variation of nightside densities [e.g., Keating *et al.*, 1980; Kasprzak *et al.*, 1993]. The eddy diffusion coefficient is prescribed in the form  $K = A/\sqrt{n}$  with units of  $\text{cm}^2 \text{ s}^{-1}$ , where  $n$  is the total number density,  $A$  is a constant, and  $K$  is the eddy diffusion coefficient (which is capped at a maxi-

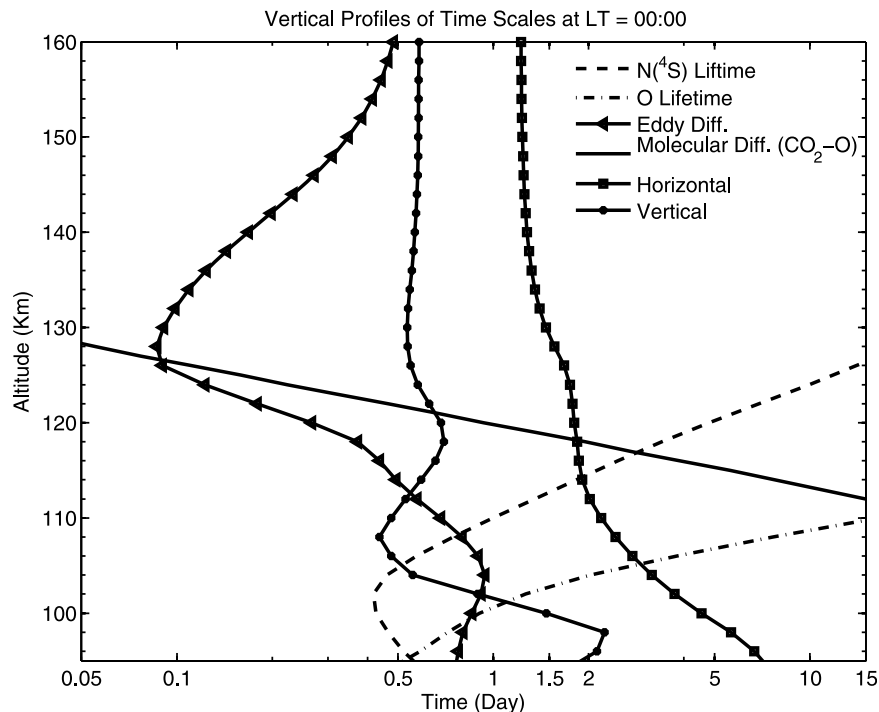
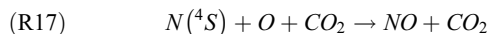


**Figure 14.** VTGCM “mean” case for VEX conditions; timescale profiles at 2.5°N (time (day) versus height (km)) for midnight.

mum value,  $K_{max}$ ) [von Zahn *et al.*, 1979]. Three  $K_{max}$  values are used for the test: (1) the maximum case is  $8.0 \times 10^7 \text{ cm}^2 \text{ s}^{-1}$ , (2) the minimum case is  $1.0 \times 10^6 \text{ cm}^2 \text{ s}^{-1}$ , and (3) the best case (which corresponds to the results discussed in section 3.2) is  $1.0 \times 10^7 \text{ cm}^2 \text{ s}^{-1}$ . The eddy diffusion profiles for this study are represented in Figure 15a and the results of the sensitivity test can be seen in Table 3. Eddy diffusion proves to be a major factor in controlling the altitude of the nightglow peaks [Bougher *et al.*, 1997; Bougher and Borucki, 1994]. For the new VTGCM, the O<sub>2</sub> IR nightglow intensity is more sensitive than the NO UV nightglow to the changing eddy diffusion coefficient. The nightglow intensities also vary with respect to the location of the sources and sinks of the nightglow layer. Lower in the atmosphere, CO<sub>2</sub> concentrations are greater, which reduces the O<sub>2</sub> IR night airglow chemical sources by increasing the deactivation of the O<sub>2</sub> ( $a^1\Delta$ ) state by CO<sub>2</sub> quenching. The NO UV nightglow intensity varies as the nightglow layer moves vertically for a similar reason, with an additional N(<sup>4</sup>S) sink being:



A larger eddy coefficient leads to reaction (R17) competing more effectively with reaction (R16) for N(<sup>4</sup>S) atoms, thereby reducing the NO\* source. The opposite happens when the eddy coefficient is minimized.

### 3.3.2. Sensitivity Tests: Wind

[65] The wind sensitivity is related to the tunable wave drag parameter which is part of the Rayleigh friction scheme. The Rayleigh friction term is implemented to approximate gravity wave momentum drag effects. This rudimentary formulation is linearly proportional to the

horizontal (2-D) wind, and is added to the momentum equation thereby controlling the magnitude of the zonal and meridional winds and ultimately the magnitude of the subsiding winds near midnight. The procedure of the wind sensitivity test is similar to the eddy diffusion sensitivity test. The wave drag timescale maximum values ( $\lambda_0$  parameter in the wave drag equation) used are as follows: (1) the maximum case is  $2 \times 10^{-4} \text{ s}^{-1}$  (providing slower winds), (2) the minimum case is  $1.25 \times 10^{-5} \text{ s}^{-1}$  (providing faster winds), and (3) the best case is  $0.5 \times 10^{-4} \text{ s}^{-1}$  (providing optimal winds and is used for all results discussed in section 3.2). The resulting evening terminator (18:00 LT) zonal wind profile for each case is represented in Figure 15b.

[66] Table 4 summarizes the results of the wind sensitivity study. These cases demonstrate that the intensities of the nightglow emissions are impacted more strongly than the altitude of the nightglow peaks. The stronger impact on the intensities is due to the SS-AS wind system that supplies the nightside with O and N(<sup>4</sup>S) atoms transported from the dayside. The nightglow intensities respond accordingly to the strength of the winds, while the nightside N(<sup>4</sup>S) peak density does not. In fact, the nightside O density and the nightside N(<sup>4</sup>S) density have opposite responses to the strength of the wind. The closer the density peaks are in altitude, the greater the loss of N(<sup>4</sup>S) through reactions (R15) and (R16). As shown in Table 4, the weaker winds provide more N(<sup>4</sup>S) (less O) on the nightside and the stronger winds yield more N(<sup>4</sup>S) and O when compared to the “best case”. This implies the drag term is most influential between 100 km and 110 km, where O density peaks. For the morphology of the nightglow emissions, the local time distribution is shifted toward the MT (ET) when there are stronger (weaker) winds. Therefore, the source of these

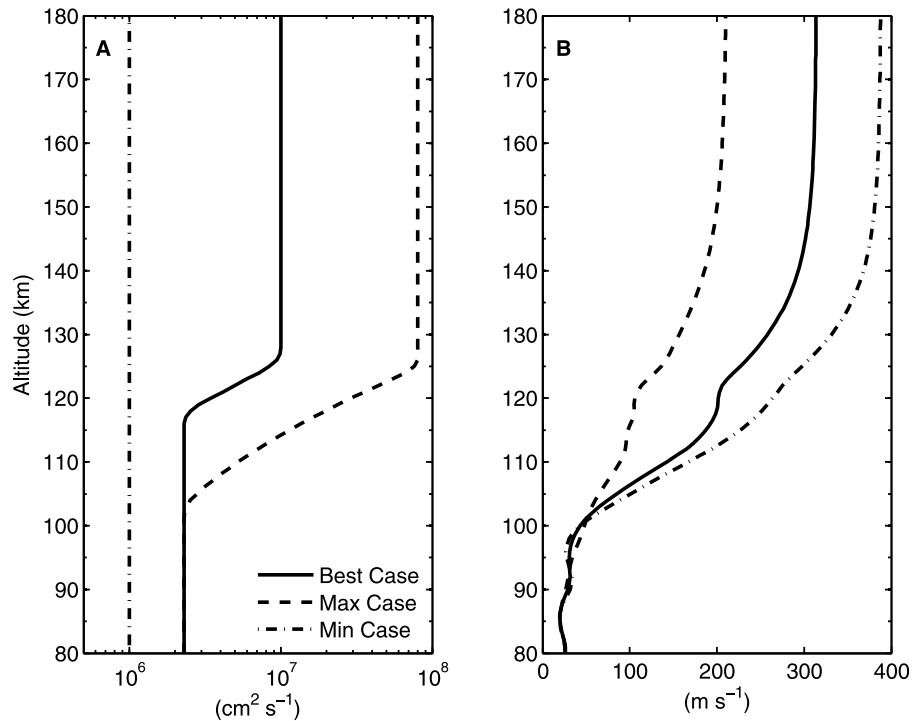


**Figure 15.** VTGCM sensitivity case parameters. (a) The three profiles for the nightside eddy diffusion sensitivity tests. (b) The three resulting evening terminator (18:00 LT) zonal wind profiles for the wind sensitivity tests.

atoms, and thus the nightglow peak brightness and location, directly depends on the strength of these winds.

[67] Furthermore, it is suggested the nightside warm region is created by dynamical heating, and Table 4 illustrates the nightside warm region's sensitivity to the wind changes. The decrease in wind results in a cooler "warm" region and it peaks 9 km lower than the "best case", while a increase in the global wind system results in the opposite response.

### 3.3.3. Sensitivity Tests: Key Chemical Reaction Rates

[68] For the three-body reaction rate (R1), modelers have been using a standard Earth value and multiplying it by a constant factor to enable the reaction rate to correspond to a CO<sub>2</sub> dominated atmosphere. Recently, this reaction has been measured in the laboratory in a CO<sub>2</sub> background atmosphere by *Jamieson et al.* [2009b]. In Table 2 the different reaction rates used in this sensitivity test are clearly stated. When the preliminary (test) (R1) rate is used a slight impact on the O density profiles is identified (~13% increase for the peak dayside density and ~12.6% increase for the peak nightside

density) within the VTGCM simulations. The change from the standard (R1) to the preliminary (test) (R1) leaves more O available on the nightside and decreases the peak O<sub>2</sub> nightglow intensity to 1.68 MR. However, the peak altitude remained at 100 km. The NO UV nightglow layer remains at 106 km, but has a slight increase in intensity to 1.9 kR.

[69] In the past, the VTGCM used an Earth based value for the three-body reaction rate (R17). This sensitivity study compares the atmospheric impacts when using this previous reaction rate (test) and a standard one based upon measurements using a CO<sub>2</sub> background atmosphere (see Table 2 and see section 2.3 for more details about the rates). By using the standard reaction rate ( $1.83 \times 10^{-32} (298/T_n)^{0.5} \text{ cm}^6 \text{ s}^{-1}$ ), which is faster, this requires fewer N and O atoms for reaction (R16) to occur at higher altitudes, thus resulting in the NO UV nightglow layer occurring higher in the atmosphere and further separated from the O<sub>2</sub> IR nightglow layer. When using the test reaction rate ( $1.1 \times 10^{-32} (300/T_n)^{0.5} \text{ cm}^6 \text{ s}^{-1}$ ), which is slower, this leads to N and O atoms recombining lower in the atmosphere. However, application of the stan-

**Table 3.** Results From the Nightside Eddy Diffusion Sensitivity Test

O <sub>2</sub> (IR)	O Den Peak (Night) (cm <sup>-3</sup> )	Altitude (km)	Peak Intensity (MR)	Nightglow Peak Altitude (km)
Best	$3.41 \times 10^{11}$	104	1.76	100
Max	$2.62 \times 10^{11}$	102	1.04	100
Min	$3.93 \times 10^{11}$	105	2.58	103
NO (UV)	N Den Peak (Night) (cm <sup>-3</sup> )	Altitude (km)	Peak Intensity (kR)	Nightglow Peak Altitude (km)
Best	$1.37 \times 10^8$	115	1.83	106
Max	$1.76 \times 10^8$	109	1.64	104
Min	$1.65 \times 10^8$	118	2.04	109

**Table 4.** Results From the Wind Sensitivity Test

O <sub>2</sub> (IR)	O Den Peak (Day) (cm <sup>-3</sup> )	Altitude (km)	O Den Peak (Night) (cm <sup>-3</sup> )	Altitude (km)	Peak Intensity (MR)	Nightglow Peak Altitude (km)
Best	$5.47 \times 10^{10}$	94	$3.41 \times 10^{11}$	104	1.76	100
Max	$5.56 \times 10^{10}$	95	$2.36 \times 10^{11}$	104	0.92	99
Min	$5.44 \times 10^{10}$	94	$3.93 \times 10^{11}$	104	2.42	101
NO (UV)	N Den Peak (Day) (cm <sup>-3</sup> )	Altitude (km)	N Den Peak (Night) (cm <sup>-3</sup> )	Altitude (km)	Peak Intensity (kR)	Nightglow Peak Altitude (km)
Best	$1.03 \times 10^8$	136	$1.37 \times 10^8$	115	1.83	106
Max	$2.17 \times 10^8$	134	$2.30 \times 10^8$	115	1.64	110
Min	$7.00 \times 10^7$	136	$1.65 \times 10^8$	115	3.56	106
T <sub>night</sub>	Peak Temperature (K)	Altitude (km)				
Best	188	103				
Max	173	94				
Min	207	105				

standard rate does not impact the NO UV nightglow layer height and the intensity increases from 1.83 kR to 1.92 kR. Reaction rate (R17) is the least important loss of N(<sup>4</sup>S) compared to reactions R16 and R15. Nevertheless, since (R17) does impact the NO UV nightglow, this chemical reaction rate is in need of a new laboratory measurement for application to Venus.

[70] In the literature, error bars are typically stated for measurements of chemical reaction rates. Thus, a careful examination of a range of reaction rates for odd N chemistry was tested using the VTGCM. Little impact was observed on the altitude of the NO UV nightglow peak [Bougher *et al.*, 1990; Fox, 1994; Fox and Sung, 2001; Krasnopolsky, 2010]. In short, the combination of the chemical reaction rates listed in Table 1 are used to create the VTGCM “mean” case.

### 3.3.4. Sensitivity Tests: Chemical Trace Species

[71] By implementing the Krasnopolsky [2010] night profiles of chemical trace species into the VTGCM, the density profiles and night airglow distributions were impacted. The trace species provide additional loss terms for the O chemistry below 95 km, which creates a narrower O density layer (see Figure 10). The more defined O density layer becomes more sensitive to the dominating reactions (e.g., (R1)), as previously discussed, resulting in a more sensitive nightglow emission layer with respect to the eddy diffusion coefficient. The O<sub>2</sub> IR nightglow layer is raised a kilometer with the trace species, and the peak intensity is decreased (by 0.2 MR). The N(<sup>4</sup>S) density plot changes slightly as well (see Figure 11). The NO UV nightglow is created in the region where the N(<sup>4</sup>S) density layer overlaps the O density layer. Since the O density layer is more sensitive to the eddy diffusion coefficient, this also creates a more variable NO UV nightglow layer. However, the NO UV nightglow layer altitude and intensity did not change with the addition of trace species.

### 3.3.5. Sensitivity Tests: Conclusions

[72] These sensitivity tests show that the wave drag parameter (impacting wind magnitudes) controls the intensity of the nightglow emissions, while eddy diffusion controls the altitude of the nightglow layers. The O<sub>2</sub> IR nightglow is more sensitive to eddy diffusion and the NO UV nightglow is more sensitive to the wave drag parameter (the strength of the global wind system). The key reaction rate tests revealed little impact on the nightglow layers

location, but slightly impacted the intensity. The addition of chemical trace species is crucial for completeness and determining the shape of the O<sub>2</sub> IR nightglow emission layer. Overall, these different responses may explain (in part) the observed variability in location and intensity of the O<sub>2</sub> IR and NO UV nightglow emissions. Moreover, the implications of the timescale plot (see Figure 14), plus the eddy diffusion and the wind sensitivity tests, point to a dynamical explanation for the lack of correlation between these concurrently observed nightglow emissions (see section 4.3) [Gérard *et al.*, 2009b].

## 4. Implications and Data Model Comparisons

[73] The latest VTGCM modeling efforts have been focused on three key VEX observations: (1) the nightside warm layer near 100 km, (2) the O<sub>2</sub> IR nightglow, and (3) the NO UV nightglow. Currently, the modeling of these key observations is unique because the VTGCM alone provides a self-consistent set of structural and dynamical fields (i.e., temperature, three component winds, major composition). These results provide confidence in the validity of the global thermospheric circulation pattern for mean conditions.

### 4.1. Nightside Temperature

[74] The first key observation is the nightside warm layer, which was first measured using stellar occultations from SPICAV [Bertaux *et al.*, 2007]. These limited VEX measurements show temperatures of ~185 K up to ~240 K for an altitude range of 95–100 km. These authors state that continued measurements are needed to establish a climatology of these temperatures and confirm a mean value in this nightside altitude region. VEX observations are being supplemented with ground-based observations which generally reveal ~95 to 100 km nightside temperatures near midnight that are cooler (~160–200 K) than the SPICAV values [Rengel *et al.*, 2008; Clancy *et al.*, 2008; Bailey *et al.*, 2008]. See Table 5 for a summary of recent observations of this nightside warm layer.

[75] The VTGCM “mean” simulation (e.g., Figure 6) shows a peak nightside temperature of 188 K at 103 km for comparison with previously discussed observations. This nightside peak temperature, absent in the earlier version of the VTGCM, is directly connected with a more realistic

**Table 5.** Summary of Temperature Measurements for the Venus Nightside Near 95 km From *Bailey et al.* [2008]

Method	Temperature (K)	Reference
1.27 $\mu\text{m}$ O <sub>2</sub> airglow	185 $\pm$ 15	<i>Connes et al.</i> [1979]
Pioneer Venus night probe deceleration	167.2	<i>Seiff and Kirk</i> [1982]
Pioneer Venus OIR	170–175	<i>Schofield and Taylor</i> [1983]
VIRA (based on OIR and probe deceleration)	168	<i>Seiff et al.</i> [1985]
CO mm lines	165–210	<i>Clancy and Muhleman</i> [1991]
1.27 $\mu\text{m}$ O <sub>2</sub> airglow	186 $\pm$ 6	<i>Crisp et al.</i> [1996]
CO mm lines	165–178	<i>Clancy et al.</i> [2003]
1.27 $\mu\text{m}$ O <sub>2</sub> airglow	193 $\pm$ 9	<i>Ohtsuki et al.</i> [2005]
Venera 15 IR Fourier spectrometer	166.4	<i>Zasova et al.</i> [2006]
SPICAV Stellar occultation	194–240	<i>Bertaux et al.</i> [2007]
Submillimeter observations with HHSMT	~160–200	<i>Rengel et al.</i> [2008]
Submillimeter observations with JCMT	~175–180	<i>Clancy et al.</i> [2008]
1.27 $\mu\text{m}$ O <sub>2</sub> airglow (intensity weighted mean)	181–196	<i>Bailey et al.</i> [2008]

4.3  $\mu\text{m}$  heating on the dayside, and the resultant enhancement of day-to-night winds. The stronger winds create a larger thermal advection and result in increased adiabatic heating near midnight. The opposite effect on the temperature occurs when the winds are weakened (see section 3.3.2). The VTGCM nightside temperature of  $\sim 190$  K near 100 km corresponds to an average case for solar minimum conditions, in accord with available spacecraft and ground-based observations (see Table 5). Continued monitoring will provide additional observations that will help confirm average nightside temperatures.

#### 4.2. O<sub>2</sub> IR Nightside Airglow

[76] The second key observation is the O<sub>2</sub> IR nightside airglow. *Gérard et al.* [2008b] created a statistical hemispheric mean map of the nadir viewed O<sub>2</sub> IR night airglow intensity which provided a maximum emission of  $\sim 3$  MR, but was later corrected to be  $\sim 1.6$  MR [*Soret et al.*, 2011]. The peak emission is located near the equator at midnight, but significant variability is shown in the distribution and intensity. In addition, *Piccioni et al.* [2009] created a similar O<sub>2</sub> IR nightglow map using an expanded data set that overlaps the one used by *Gérard et al.* [2008b] for their map. The maximum vertical emission rate is 1.2 MR and is located at the antisolar point slightly below the equator. The *Soret et al.* [2011] O<sub>2</sub> IR nightglow map illustrated a hemispheric average intensity of  $\sim 0.5$  MR, while *Piccioni et al.* [2009] calculated a mean total vertical emission rate of 0.52 MR. *Gérard et al.* [2009a] and *Soret et al.* [2011] have been able to deduce nightside O density profiles (consistent with O<sub>2</sub> IR nightglow maps) which provide additional valuable constraints for modelers.

[77] The *Gérard et al.* [2008b] one-dimensional chemical diffusive model can replicate the O<sub>2</sub> IR night airglow peak altitude. This nightside one-dimensional model has two main tunable parameters: the downward flux of atomic oxygen and the eddy diffusion coefficient. Using these parameters, they were able to match the observed O<sub>2</sub> IR night airglow limb profiles. Specifically when modeling the O<sub>2</sub> IR night airglow, they keep the atomic oxygen downward flux at 130 km relatively constant near  $3.5 \times 10^{12} \text{ cm}^{-2} \text{ s}^{-1}$  and vary the eddy diffusion coefficient ( $A = 4 \times 10^{12}$ ). *Gérard et al.* [2008b] show one of their selected 1-D model fits for a single orbit. The O density peak obtained when nearly matching the night airglow layer is  $1.8 \times 10^{11} \text{ cm}^{-3}$  at 104 km.

[78] The new VTGCM produces O<sub>2</sub> nightglow intensities and O density values within the ranges stated by *Gérard et al.* [2008b] and *Gérard et al.* [2009a]. In addition, the produced O<sub>2</sub> nightglow intensities are in excellent accord with mean values derived in those studies. The VTGCM nightside O density peaks at 104 km, compared to VEX mean altitude of 102 km [*Soret et al.*, 2009, 2011], with a value of  $3.41 \times 10^{11} \text{ cm}^{-3}$ , compared to the VEX value of  $2 \times 10^{11} \text{ cm}^{-3}$ . The corresponding net dayside column integrated production is  $2.34 \times 10^{12} \text{ cm}^{-2} \text{ s}^{-1}$ , while the 1-D model uses a flux of  $3.5 \times 10^{12} \text{ cm}^{-2} \text{ s}^{-1}$ . An earlier estimate was made using a 1-D photochemical-diffusive transport model and a downward flux of oxygen of  $5 \times 10^{11} \text{ cm}^{-2} \text{ s}^{-1}$ , which corresponds to a limb profile from VEX orbit 76 at 35°N [*Drossart et al.*, 2007]. This flux had an associated  $A = 2 \times 10^{12}$  and O density peak of  $1.3 \times 10^{11} \text{ cm}^{-3}$  at 100 km [*Drossart et al.*, 2007]. The O<sub>2</sub> nightglow peak volume emission rate produced by the VTGCM is located at  $\sim 100$  km with an integrated vertical intensity of 1.76 MR, which is located near 00:00 LT. As mentioned earlier, the VTGCM nightglow result is for a yield of 75% in reaction (R1); a 100% yield would provide a VTGCM peak vertical intensity of 2.37 MR. Statistically averaged observations reveal the mean peak intensity to be 1.6 MR at 96 km and on average seen at midnight [*Soret et al.*, 2009, 2011; *Gérard et al.*, 2008b]. The VTGCM produces a hemispheric average intensity of 0.51–0.63 MR (averaged over a limited nightside box) when compared to VEX 0.47 MR [*Soret et al.*, 2011]. For the VTGCM sensitivity test results, we notice the O<sub>2</sub> IR night airglow layer is controlled by two processes. The altitude is mainly controlled by eddy diffusion and the intensity of the nightglow is controlled by the winds. The stronger the winds, the more O is transported from the dayside to the nightside resulting in a more intense emission with a corresponding depletion of O on the dayside.

#### 4.3. NO UV Nightside Airglow

[79] The third key observation is the NO UV night airglow. *Bougher et al.* [1990] published results for solar minimum simulations from an older version of the VTGCM. The older VTGCM adopted different values for certain parameters and did not include all the updates the new VTGCM has incorporated. A few of the modified parameters are the newly specified eddy diffusion coefficient, the prescribed RSZ wind profile, updated chemical reaction

rates, and near-IR heating and 15  $\mu\text{m}$  cooling rates. Nevertheless, comparing case 5a from *Bougher et al.* [1990] to the new VTGCM best case can be insightful. Case 5a produced a dayside N density of  $2.6 \times 10^7 \text{ cm}^{-3}$  at 135 km with a corresponding nightside peak density of  $1.8 \times 10^8 \text{ cm}^{-3}$  at 112 km. This case produced a net dayside column production of  $1.05 \times 10^9 \text{ cm}^{-2} \text{ s}^{-1}$ . The nightglow dark disk average was 0.156 kR with a peak intensity of 0.42 kR for the (0, 1)  $\delta$  band only. Recall that this  $\delta$  band is  $\sim 20\%$  of the total spectrum and was calculated in order to be comparable with the typical PVO observations.

[80] VEX global maps of the statistical mean NO UV night airglow structure do not yet exist, unlike the O<sub>2</sub> IR night airglow. However, *Gérard et al.* [2008c] employed their 1-D model to simulate individual NO UV nightglow limb profiles, just as for the O<sub>2</sub> IR night airglow. This study used several values for  $A$ , the variable prescribed in the calculation for the eddy diffusion coefficient, to reproduce three limb profiles ( $7.4 \times 10^{11}$ ,  $4 \times 10^{12}$ , and 0). The downward nitrogen flux at 130 km ranges between  $1 \times 10^8 \text{ cm}^{-2} \text{ s}^{-1}$  and  $4 \times 10^9 \text{ cm}^{-2} \text{ s}^{-1}$ , but has a typical value of  $2 \times 10^9 \text{ cm}^{-2} \text{ s}^{-1}$ . For one specific orbit (Orbit 320), the N(<sup>4</sup>S) nightside density is  $2 \times 10^8 \text{ cm}^{-3}$  at 122 km [*Gérard et al.*, 2008c]. *Cox* [2010] has calculated a hemispheric averaged  $\sim 1.2$  kR for all bands ( $\delta$  and  $\gamma$  bands) and identified the mean altitude for the NO UV night airglow to be  $114.8 \pm 5.8$  km but can vary from 95 to 132 km [*Gérard et al.*, 2008c; *Cox*, 2010].

[81] The new VTGCM simulates a nightside N(<sup>4</sup>S) density peak value of  $1.37 \times 10^8 \text{ cm}^{-3}$  at 115 km with a peak volume emission rate of  $1.23 \times 10^3$  (photon  $\text{cm}^{-3} \text{ s}^{-1}$ ) located at 106 km. The corresponding peak nightglow intensity for solar minimum conditions is 1.83 kR for the combined  $\delta$  and  $\gamma$  bands. This peak intensity is similar to the old VTGCM value ( $0.42 \text{ kR} \times 5 = 2.1 \text{ kR}$ ) [*Bougher et al.*, 1990]. The simulated peak nightside N(<sup>4</sup>S) density value is a nearly a factor of 1.5 times smaller than that of *Bougher et al.* [1990] and *Gérard et al.* [2008c] values ( $1.37 \times 10^8$  versus  $2 \times 10^8 \text{ cm}^{-3}$ ). Furthermore, the new VTGCM net day column integrated production ( $1.58 \times 10^{10}$ ) is 15 times greater than that of *Bougher et al.* [1990] and a factor of 8 greater than *Gérard et al.* [2008c]. The simulated peak nightglow altitude ( $\sim 106$  km) is at the lower end of the established range; i.e., the range for the peak altitude is 95–132 km with a mean of 113 km [*Gérard et al.*, 2008c]. Abel inversion of 725 deconvolved limb profiles [*Cox*, 2010] indicates that the peak volume emission rate is located at  $114.8 \pm 5.8$  km. The hemispheric averaged intensity on the nightside is 1.2 kR while the new VTGCM simulates a smaller intensity of 0.68 kR, but once again similar to the old VTGCM value [*Bougher et al.*, 1990; *Gérard et al.*, 2008c; *Cox*, 2010]. Reasonable chemical reaction rate tests (i.e., within established measurement error bars) have been conducted to increase the simulated intensity and raise the nightglow emission layer; little variation of these nightglow features has resulted. The simulated NO UV night airglow distribution shows a maximum near 01:00 LT. The NO UV night airglow peak emission is not shifted closer to 02:00 LT because the NO UV emission layer is too close in altitude to the O<sub>2</sub> IR emission layer. The calculated separation of these nightglow layers in altitude is  $\sim 7$  km and the corresponding RSZ wind change is not dramatic (see Figure 8).

If the altitude separation of these two nightglow layers is increased to 17–20 km, the RSZ wind approaches  $30 \text{ m s}^{-1}$  in the NO UV nightglow layer. This would provide a greater shift in local time for the NO UV nightglow compared to the O<sub>2</sub> IR nightglow.

## 5. Conclusions

[82] VEX is continuing to make observations that are contributing to a better understanding of Venus' global dynamics in the middle and upper atmosphere. In particular, the VEX O<sub>2</sub> IR nightglow statistical maps are helping to constrain global models and characterize average conditions that permit SS-AS and RSZ components of the upper atmosphere circulation to be estimated. The construction of a NO UV nightglow statistical map is in progress and will also help constrain dynamics in models in a higher altitude region above the O<sub>2</sub> IR nightglow layer. Variability about these statistically mean conditions can be used to characterize the fluctuations of the SS-AS and RSZ wind components at different altitude levels: 90–110 km (O<sub>2</sub>) and 95–132 km (NO).

[83] The VTGCM model is currently able to provide a self consistent view of Venus' time averaged global dynamics in the middle and upper atmosphere. The VTGCM reproduces a nightside warm spot of 188 K at 103 km, consistent with available ground-based and spacecraft observations showing an average of  $\sim 190$  K at 100 km. Furthermore, the simulated VTGCM O<sub>2</sub> IR nightglow intensity and altitude is a good representation of mean conditions. However, the simulated NO UV nightglow layer altitude is 8–10 km too low and its peak intensity is located near 01:00 LT. If the NO UV layer is raised to  $\sim 115$ –120 km, the layer is then positioned into a stronger RSZ wind regime and the peak emission will be located near 02:00 LT, as observed.

[84] With the VTGCM successfully representing mean VEX observations, sensitivity studies were performed with the two tunable parameters (nightside eddy diffusion coefficient and the wave drag term). The results of the sensitivity studies imply there are at least two sources of variability (eddy diffusion and the vertical winds) impacting nightside emissions. These two sources do not always impact both night airglow emissions equally. The VTGCM simulations clearly show eddy diffusion dominates the region where O<sub>2</sub> IR nightglow emission peaks and the vertical winds dominate the region where NO UV nightglow peaks, both near midnight. These sensitivity tests reveal why the two nightglow layers would vary independently of each other. The dynamical consequences of the eddy diffusion variability and the vertical wind variability can only be simulated utilizing a multidimensional dynamical model. *Gérard et al.* [2009a] measured the O<sub>2</sub> IR and NO UV night airglows simultaneously and did not find a spatial correlation between the two nightglows. They explained this lack of correlation by the two different wind regimes encountered by the separate nightglow layers. In VTGCM simulations, it is crucial to prescribe a very weak RSZ below  $\sim 110$  km and a rapidly growing RSZ above  $\sim 110$  km to  $\sim 130$  km to model the nightglow peak emissions at the observed local times. The VTGCM can demonstrate why this noncorrelation exists, provided that the distinct nightglow layers are separated in altitude by at least  $\sim 15$  km.

[85] Future work will examine in more detail the horizontal and vertical O density distributions on the nightside while replacing the Rayleigh friction scheme with a new gravity wave momentum deposition formulation in the VTGCM. Soret *et al.* [2011] have compiled the VIRTIS observations of the O<sub>2</sub> IR nightglow and derived corresponding O density maps. The density maps can provide a detailed constraint for the VTGCM on the nightside since atomic oxygen is the common reactant between the O<sub>2</sub> IR and NO UV nightglow emissions. This data-model comparison may provide insight into why the NO UV nightglow layer simulated by the VTGCM is low in altitude compared to observations. A gravity wave momentum deposition scheme will be included to simulate disturbances from the lower atmosphere. Wave-like features have been observed by VEX and are thought to be a main contributor to Venus' atmospheric variability and act as the decelerator/accelerator for the general circulation [e.g., Markiewicz *et al.*, 2007; Peralta *et al.*, 2008; Sánchez-Lavega *et al.*, 2008; Garcia *et al.*, 2009].

[86] **Acknowledgments.** We thank D. L. Huestis for useful discussions concerning this research. This research was sponsored in part by NASA Planetary Atmospheres grant NNX08AG18G. Both Bougher and Rafkin acknowledge NASA Venus Express Participating Scientist support. NSF grant AST-0406650 also sponsored a portion of this research. Computer resources were supplied by the National Center for Atmospheric Research, which is sponsored by the National Science Foundation. Last, we thank two reviewers for their detailed and constructive comments.

## References

- Alexander, M. J. (1992), A mechanism for the Venus thermospheric super-rotation, *Geophys. Res. Lett.*, *19*, 2207–2210, doi:10.1029/92GL02110.
- Anicich, V. G. (1993), Evaluated bimolecular ion-molecule gas phase kinetics of positive ions for use in modeling planetary atmospheres, cometary comae, and interstellar clouds, *J. Phys. Chem. Ref. Data*, *22*, 1469–1569, doi:10.1063/1.555940.
- Bailey, J., S. Chamberlain, D. Crisp, and V. S. Meadows (2008), Near infrared imaging spectroscopy of Venus with the Anglo-Australian Telescope, *Planet. Space Sci.*, *56*, 1385–1390, doi:10.1016/j.pss.2008.03.006.
- Baulch, D. L., D. Drysdale, D. G. Horne, and A. C. Lloyd (1973), Homogeneous gas phase reactions of the H<sub>2</sub>-N<sub>2</sub>-O<sub>2</sub> system, in *Evaluated Kinetic Data for High Temperature Reactions*, vol. 2, pp. 1–557, Chem. Rubber Co. Press, Cleveland, Ohio.
- Baulch, D. L., R. A. Cox, R. F. Hampson, J. A. Kerr, J. Troe, and R. T. Watson (1980), Evaluated kinetic and photochemical data for atmospheric chemistry, *J. Phys. Chem. Ref. Data*, *9*, 295–471, doi:10.1063/1.555619.
- Bertaux, J., *et al.* (2007), A warm layer in Venus' cryosphere and high-altitude measurements of HF, HCl, H<sub>2</sub>O and HDO, *Nature*, *450*, 646–649, doi:10.1038/nature05974.
- Bougher, S. W., and W. J. Borucki (1994), Venus O<sub>2</sub> visible and IR nightglow: Implications for lower thermosphere dynamics and chemistry, *J. Geophys. Res.*, *99*, 3759–3776, doi:10.1029/93JE03431.
- Bougher, S. W., R. E. Dickinson, E. C. Ridley, R. G. Roble, A. F. Nagy, and T. E. Cravens (1986), Venus mesosphere and thermosphere. II - Global circulation, temperature, and density variations, *Icarus*, *68*, 284–312, doi:10.1016/0019-1035(86)90064-4.
- Bougher, S. W., R. G. E. Roble, R. E. Dickinson, and E. C. Ridley (1988), Venus mesosphere and thermosphere. III - Three-dimensional general circulation with coupled dynamics and composition, *Icarus*, *73*, 545–573, doi:10.1016/0019-1035(88)90064-4.
- Bougher, S. W., J.-C. Gérard, A. I. F. Stewart, and C. G. Fesen (1990), The Venus nitric oxide night airglow: Model calculations based on the Venus Thermospheric General Circulation Model, *J. Geophys. Res.*, *95*, 6271–6284, doi:10.1029/JA095iA05p06271.
- Bougher, S. W., D. M. Hunten, and R. G. Roble (1994), CO<sub>2</sub> cooling in terrestrial planet thermospheres, *J. Geophys. Res.*, *99*, 14,609–14,622, doi:10.1029/94JE01088.
- Bougher, S. W., M. J. Alexander, and H. G. Mayr (1997), Upper Atmosphere Dynamics: Global Circulation and Gravity Waves, in *Venus II: Geology, Geophysics, Atmosphere, and Solar Wind Environment*, edited by S. W. Bougher, D. M. Hunten, and R. J. Phillips, pp. 259–291, Univ. of Ariz. Press, Tucson.
- Bougher, S. W., S. Engel, R. G. Roble, and B. Foster (1999), Comparative terrestrial planet thermospheres: 2. Solar cycle variation of global structure and winds at equinox, *J. Geophys. Res.*, *104*, 16,591–16,611, doi:10.1029/1998JE001019.
- Bougher, S. W., R. G. Roble, and T. Fuller-Rowell (2002), Simulations of the Upper Atmospheres of the Terrestrial Planets, in *Atmospheres in the Solar System: Comparative Aeronomy*; *Geophys. Monogr. Ser.*, vol. 130, edited by M. Mendillo, A. Nagy, and J. H. Waite, pp. 261–288, AGU, Washington, D. C.
- Bougher, S. W., S. Rafkin, and P. Drossart (2006), Dynamics of the Venus upper atmosphere: Outstanding problems and new constraints expected from Venus Express, *Planet. Space Sci.*, *54*, 1371–1380, doi:10.1016/j.pss.2006.04.023.
- Bougher, S. W., P. Blevy, M. Combi, J. L. Fox, I. Mueller-Wodarg, A. Ridley, and R. G. Roble (2008), Neutral upper atmosphere and ionosphere modeling, *Space Sci. Rev.*, *139*, 107–141, doi:10.1007/s11214-008-9401-9.
- Brecht, A., S. Bougher, S. Rafkin, and B. Foster (2007), Venus upper atmosphere winds traced by night airglow distributions: NCAR VTGCM simulations, *Eos Trans. AGU*, *88*(52), Fall Meet. Suppl., Abstract P33B-1299.
- Brecht, A., S. W. Bougher, C. D. Parkinson, Y. L. Yung, and S. C. Rafkin (2009), Understanding the variability of nightside temperatures and airglow emissions in Venus' middle and upper atmosphere: NCAR VTGCM simulations, *Eos Trans. AGU*, *90*(52), Fall Meet. Suppl., Abstract P33A-1267.
- Campbell, I. M., and C. N. Gray (1973), Rate constants for O(<sup>3</sup>P) recombination and association with N(<sup>4</sup>S), *Chem. Phys. Lett.*, *18*, 607–609, doi:10.1016/0009-2614(73)80479-8.
- Campbell, I. M., and B. A. Thrush (1966), Behaviour of carbon dioxide and nitrous oxide in active nitrogen, *Trans. Faraday Soc.*, *62*, 3366–3374, doi:10.1039/tf9666203366.
- Clancy, R. T., and D. O. Muhleman (1991), Long-term (1979–1990) changes in the thermal, dynamical, and compositional structure of the Venus mesosphere as inferred from microwave spectral line observations of <sup>12</sup>CO, <sup>13</sup>CO, and C<sup>18</sup>O, *Icarus*, *89*, 129–146, doi:10.1016/0019-1035(91)90093-9.
- Clancy, R. T., B. J. Sandor, and G. H. Moriarty-Schieven (2003), Observational definition of the Venus mesopause: Vertical structure, diurnal variation, and temporal instability, *Icarus*, *161*, 1–16, doi:10.1016/S0019-1035(02)00022-2.
- Clancy, R. T., B. J. Sandor, and G. H. Moriarty-Schieven (2008), Venus upper atmospheric CO, temperature, and winds across the afternoon/evening terminator from June 2007 JCMT sub-millimeter line observations, *Planet. Space Sci.*, *56*, 1344–1354, doi:10.1016/j.pss.2008.05.007.
- Collet, A., C. Cox, and J. C. Gérard (2010), Two-dimensional time-dependent model of the transport of minor species in the Venus night side upper atmosphere, *Planet. Space Sci.*, *58*, 1857–1867, doi:10.1016/j.pss.2010.08.016.
- Connes, P., J. F. Noxon, W. A. Traub, and N. P. Carleton (1979), O<sub>2</sub> (<sup>1</sup>Δ) emission in the day and night airglow of Venus, *Astrophys. J.*, *233*, L29–L32, doi:10.1086/183070.
- Cox, C. (2010), Analyse et modélisation des émissions ultraviolettes de l'atmosphère de Venus et de Mars à l'aide des instruments SPICAM et SPICAV, Ph.D. thesis, Univ. de Liège, Liège, France.
- Crisp, D., V. S. Meadows, B. Bézard, C. de Bergh, J. Maillard, and F. P. Mills (1996), Ground-based near-infrared observations of the Venus nightside: 1.27-μm O<sub>2</sub> (<sup>1</sup>Δ<sub>g) airglow from the upper atmosphere, *J. Geophys. Res.*, *101*, 4577–4593, doi:10.1029/95JE03136.</sub>
- Dalgarno, A., J. F. Babb, and Y. Sun (1992), Radiative association in planetary atmospheres, *Planet. Space Sci.*, *40*, 243–246, doi:10.1016/0032-0633(92)90062-S.
- Deming, D., and M. J. Mumma (1983), Modeling of the 10-micron natural laser emission from the mesospheres of Mars and Venus, *Icarus*, *55*, 356–368, doi:10.1016/0019-1035(83)90108-2.
- Dickinson, R. E. (1972), Infrared radiative heating and cooling in the Venusian mesosphere. I. Global mean radiative equilibrium, *J. Atmos. Sci.*, *29*, 1531–1556, doi:10.1175/1520-0469(1972)029<1531:IRHACI>2.0.CO;2.
- Dickinson, R. E., and S. W. Bougher (1986), Venus mesosphere and thermosphere: 1. Heat budget and thermal structure, *J. Geophys. Res.*, *91*, 70–80, doi:10.1029/JA091iA01p00070.
- Dickinson, R. E., and E. C. Ridley (1972), Numerical solution for the composition of a thermosphere in the presence of a steady subsolar to-antisolar circulation with application to Venus, *J. Atmos. Sci.*, *29*(8), 1557–1570, doi:10.1175/1520-0469(1972)029<1557:NSFTCO>2.0.CO;2.

- Dickinson, R. E., and E. C. Ridley (1977), Venus mesosphere and thermosphere temperature structure. II - Day-night variations, *Icarus*, *30*, 163–178, doi:10.1016/0019-1035(77)90130-0.
- Drossart, P., et al. (2007), A dynamic upper atmosphere of Venus as revealed by VIRTIS on Venus Express, *Nature*, *450*, 641–645, doi:10.1038/nature06140.
- Fehsenfeld, F. C., D. B. Dunkin, and E. E. Ferguson (1970), Rate constants for the reaction of CO<sub>2</sub> with O, O<sub>2</sub> and NO; N<sub>2</sub><sup>+</sup> with O and NO; and O<sub>2</sub><sup>+</sup> with NO, *Planet. Space Sci.*, *18*, 1267–1269, doi:10.1016/0032-0633(70)90216-3.
- Feldman, P. D., H. W. Moos, J. T. Clarke, and A. L. Lane (1979), Identification of the UV nightglow from Venus, *Nature*, *279*, doi:10.1038/279221a0.
- Fox, J. L. (1988), Heating efficiencies in the thermosphere of Venus reconsidered, *Planet. Space Sci.*, *36*, 37–46, doi:10.1016/0032-0633(88)90144-4.
- Fox, J. L. (1994), Rate coefficient for the reaction N + NO, *J. Geophys. Res.*, *99*, 6273–6276, doi:10.1029/93JA03299.
- Fox, J. L., and K. Y. Sung (2001), Solar activity variations of the Venus thermosphere/ionosphere, *J. Geophys. Res.*, *106*, 21,305–21,335, doi:10.1029/2001JA000069.
- Fox, J. L., M. I. Galand, and R. E. Johnson (2008), Energy deposition in planetary atmospheres by charged particles and solar photons, *Space Sci. Rev.*, *139*, 3–62, doi:10.1007/s11214-008-9403-7.
- García, R. F., P. Drossart, G. Piccioni, M. López-Valverde, and G. Occhipinti (2009), Gravity waves in the upper atmosphere of Venus revealed by CO<sub>2</sub> nonlocal thermodynamic equilibrium emissions, *J. Geophys. Res.*, *114*, E00B32, doi:10.1029/2008JE003073.
- Gérard, J. C., A. I. F. Stewart, and S. W. Bougher (1981), The altitude distribution of the Venus ultraviolet nightglow and implications on vertical transport, *Geophys. Res. Lett.*, *8*, 633–636, doi:10.1029/GL008i006p00633.
- Gérard, J., B. Hubert, V. I. Shematovich, D. V. Bisikalo, and G. R. Gladstone (2008a), The Venus ultraviolet oxygen dayglow and aurora: Model comparison with observations, *Planet. Space Sci.*, *56*, 542–552, doi:10.1016/j.pss.2007.11.008.
- Gérard, J. C., A. Saglam, G. Piccioni, P. Drossart, C. Cox, S. Erard, R. Hueso, and A. Sánchez-Lavega (2008b), Distribution of the O<sub>2</sub> infrared nightglow observed with VIRTIS on board Venus Express, *Geophys. Res. Lett.*, *35*, L02207, doi:10.1029/2007GL032021.
- Gérard, J.-C., C. Cox, A. Saglam, J.-L. Bertaux, E. Villard, and C. Nehmé (2008c), Limb observations of the ultraviolet nitric oxide nightglow with SPICAV on board Venus Express, *J. Geophys. Res.*, *113*, E00B03, doi:10.1029/2008JE003078.
- Gérard, J. C., A. Saglam, G. Piccioni, P. Drossart, F. Montmessin, and J. Bertaux (2009a), Atomic oxygen distribution in the Venus mesosphere from observations of O<sub>2</sub> infrared airglow by VIRTIS-Venus Express, *Icarus*, *199*, 264–272, doi:10.1016/j.icarus.2008.09.016.
- Gérard, J. C., C. Cox, L. Soret, A. Saglam, G. Piccioni, J. Bertaux, and P. Drossart (2009b), Concurrent observations of the ultraviolet nitric oxide and infrared O<sub>2</sub> nightglow emissions with Venus Express, *J. Geophys. Res.*, *114*, E00B44, doi:10.1029/2009JE003371.
- Gérard, J. C., L. Soret, A. Saglam, G. Piccioni, and P. Drossart (2010), The distributions of the OH Meinel and O<sub>2</sub>(a<sup>1</sup>Δ – X<sup>3</sup>Σ) nightglow emissions in the Venus mesosphere based on VIRTIS observations, *Adv. Space Res.*, *45*, 1268–1275, doi:10.1016/j.asr.2010.01.022.
- Gilli, G., M. A. López-Valverde, P. Drossart, G. Piccioni, S. Erard, and A. Cardesin Moineo (2009), Limb observations of CO<sub>2</sub> and CO non-LTE emissions in the Venus atmosphere by VIRTIS/Venus Express, *J. Geophys. Res.*, *114*, E00B29, doi:10.1029/2008JE003112.
- Goldstein, J. J., M. J. Mumma, T. Kostiuk, D. Deming, F. Espenak, and D. Zipoy (1991), Absolute wind velocities in the lower thermosphere of Venus using infrared heterodyne spectroscopy, *Icarus*, *94*, 45–63, doi:10.1016/0019-1035(91)90140-0.
- Gordiets, B. F., and V. I. Panchenko (1983), Nonequilibrium infrared emission and the natural laser effect in the Venus and Mars atmospheres, *Cosmic Res.*, Engl. Transl., *21*, 725–734.
- Gougousi, T. (1997), Electron-ion recombination rate coefficient measurements in a flowing afterglow plasma, *Chem. Phys. Lett.*, *265*, 399–403, doi:10.1016/S0009-2614(96)01488-1.
- Hampson, R. F., Jr. (1980), Chemical kinetic and photochemical data sheets for atmospheric reactions, *Rep. FAA-EE-80-17*, U.S. Dep. of Transp., FAA Off. of Environ. and Energy, High Altitude Pollut. Program, Washington, D. C.
- Hedin, A. E., H. B. Niemann, W. T. Kasprzak, and A. Seiff (1983), Global empirical model of the Venus thermosphere, *J. Geophys. Res.*, *88*, 73–83, doi:10.1029/JA088iA01p00073.
- Herron, J. (1999), Evaluated chemical kinetics data for reactions of N(<sup>2</sup>D) N(<sup>2</sup>P), and N<sub>2</sub>(A<sup>3</sup>Σ<sub>g</sub><sup>+</sup>) in the gas phase, *J. Phys. Chem. Ref. Data*, *28*, 1453–1483, doi:10.1063/1.556043.
- Hierl, P. M., I. Dotan, J. V. Seeley, J. M. van Doren, R. A. Morris, and A. A. Viggiano (1997), Rate constants for the reactions of O<sup>+</sup> with N<sub>2</sub> and O<sub>2</sub> as a function of temperature (300–1800 K), *J. Chem. Phys.*, *106*, 3540–3544, doi:10.1063/1.473450.
- Hueso, R., A. Sánchez-Lavega, G. Piccioni, P. Drossart, J. C. Gérard, I. Khatuntsev, L. Zasova, and A. Migliorini (2008), Morphology and dynamics of Venus oxygen airglow from Venus Express/Visible and Infrared Thermal Imaging Spectrometer observations, *J. Geophys. Res.*, *113*, E00B02, doi:10.1029/2008JE003081.
- Huestis, D. L. (2002), Current laboratory experiments for planetary aeronomy, in *Atmospheres in the Solar System: Comparative Aeronomy*, *Geophys. Monogr. Ser.*, vol. 130, edited by M. Mendillo, A. Nagy, and J. H. Waite, pp. 245–258, AGU, Washington, D. C.
- Jamieson, C., R. M. Garcia, D. A. Pejakovic, and K. S. Kalogerakis (2009a), Oxygen atom recombination in carbon dioxide atmospheres, paper presented at Meeting Abstracts, AAS, Div. for Planet. Sci., Am. Astron. Soc., Fajardo, Puerto Rico.
- Jamieson, C. S., R. M. Garcia, D. Pejakovic, and K. Kalogerakis (2009b), The kinetics of oxygen atom recombination in the presence of carbon dioxide, *Eos Trans. AGU*, *90*(52), Fall Meet. Suppl., Abstract P51D-1156.
- Kasprzak, W. T., A. E. Hedin, H. G. Mayr, and H. B. Niemann (1988), Wavelike perturbations observed in the neutral thermosphere of Venus, *J. Geophys. Res.*, *93*, 11,237–11,245, doi:10.1029/JA093iA10p11237.
- Kasprzak, W. T., H. B. Niemann, A. E. Hedin, S. W. Bougher, and D. M. Hunten (1993), Neutral composition measurements by the Pioneer Venus Neutral Mass Spectrometer during Orbiter re-entry, *Geophys. Res. Lett.*, *20*, 2747–2750, doi:10.1029/93GL02241.
- Kasprzak, W. T., G. M. Keating, N. C. Hsu, A. I. F. Stewart, W. B. Colwell, and S. W. Bougher (1997), Solar activity behavior of the thermosphere, in *Venus II: Geology, Geophysics, Atmosphere, and Solar Wind Environment*, edited by S. W. Bougher, D. M. Hunten, and R. J. Phillips, p. 225–257, Univ. of Ariz. Press, Tucson.
- Keating, G. M., F. W. Taylor, J. Y. Nicholson, and E. W. Hinson (1979), Short-term cyclic variations and diurnal variations of the Venus upper atmosphere, *Science*, *205*, 62–64, doi:10.1126/science.205.4401.62.
- Keating, G. M., J. Y. Nicholson, and L. R. Lake (1980), Venus upper atmosphere structure, *J. Geophys. Res.*, *85*, 7941–7956, doi:10.1029/JA085iA13p07941.
- Keating, G. M., J. L. Bertaux, S. W. Bougher, R. E. Dickinson, T. E. Cravens, and A. E. Hedin (1985), Models of Venus neutral upper atmosphere—Structure and composition, *Adv. Space Res.*, *5*, 117–171, doi:10.1016/0273-1177(85)90200-5.
- Krasnopolsky, V. A. (2010), Venus night airglow: Ground-based detection of OH, observations of O<sub>2</sub> emissions, and photochemical model, *Icarus*, *207*, 17–27, doi:10.1016/j.icarus.2009.10.019.
- Lellouch, E., T. Clancy, D. Crisp, A. J. Kliore, D. Titov, and S. W. Bougher (1997), Monitoring of mesospheric structure and dynamics, in *Venus II: Geology, Geophysics, Atmosphere, and Solar Wind Environment*, edited by S. W. Bougher, D. M. Hunten, and R. J. Phillips, pp. 295–324, Univ. of Ariz. Press, Tucson.
- López-Valverde, M. A., P. Drossart, R. Carlson, R. Mehlman, and M. Roos-Serote (2007), Non-LTE infrared observations at Venus: From NIMS/Galileo to VIRTIS/Venus Express, *Planet. Space Sci.*, *55*, 1757–1771, doi:10.1016/j.pss.2007.01.008.
- Maillard, J., E. Lellouch, J. Crovisier, C. de Bergh, and B. Bézard (1995), Carbon monoxide 4.7 μm emission: A new dynamical probe of Venus' thermosphere, *Bull. Am. Astron. Soc.*, *27*, 1080.
- Markiewicz, W. J., D. V. Titov, S. S. Limaye, H. U. Keller, N. Ignatiev, R. Jaumann, N. Thomas, H. Michalik, R. Moissl, and P. Russo (2007), Morphology and dynamics of the upper cloud layer of Venus, *Nature*, *450*, 633–636, doi:10.1038/nature06320.
- Massie, S. T., D. M. Hunten, and D. R. Sowell (1983), Day and night models of the Venus thermosphere, *J. Geophys. Res.*, *88*, 3955–3969, doi:10.1029/JA088iA05p03955.
- Mehr, F. J., and M. A. Biondi (1969), Electron temperature dependence of recombination of O<sub>2</sub><sup>+</sup> and N<sub>2</sub><sup>+</sup> ions with electrons, *Phys. Rev.*, *181*, 264–271, doi:10.1103/PhysRev.181.264.
- Midey, A. J., and A. A. Viggiano (1999), Rate constants for the reaction of O<sub>2</sub><sup>+</sup> with NO from 300 to 1400 K, *J. Chem. Phys.*, *110*, 10,746–10,748, doi:10.1063/1.479017.
- Moissl, R., et al. (2009), Venus cloud top winds from tracking UV features in Venus Monitoring Camera images, *J. Geophys. Res.*, *114*, E00B31, doi:10.1029/2008JE003117.
- Nair, H., M. Allen, A. D. Anbar, Y. L. Yung, and R. T. Clancy (1994), A photochemical model of the martian atmosphere, *Icarus*, *111*, 124–150, doi:10.1006/icar.1994.1137.
- Ohtsuki, S., N. Iwagami, H. Sagawa, Y. Kasaba, M. Ueno, and T. Imamura (2005), Ground-based observation of the Venus 1.27-μm O<sub>2</sub> airglow, *Adv. Space Res.*, *36*, 2038–2042, doi:10.1016/j.asr.2005.05.078.



- Ohtsuki, S., N. Iwagami, H. Sagawa, M. Ueno, Y. Kasaba, T. Imamura, and E. Nishihara (2008), Imaging spectroscopy of the Venus 1.27- $\mu\text{m}$  O<sub>2</sub> airglow with ground-based telescopes, *Adv. Space Res.*, *41*, 1375–1380, doi:10.1016/j.asr.2007.10.014.
- Pätzold, M., et al. (2007), The structure of Venus' middle atmosphere and ionosphere, *Nature*, *450*, 657–660, doi:10.1038/nature06239.
- Peralta, J., R. Hueso, A. Sánchez-Lavega, G. Piccioni, O. Lanciano, and P. Drossart (2008), Characterization of mesoscale gravity waves in the upper and lower clouds of Venus from VEX-VIRTIS images, *J. Geophys. Res.*, *113*, E00B18, doi:10.1029/2008JE003185.
- Piccioni, G., et al. (2008), First detection of hydroxyl in the atmosphere of Venus, *Astron. Astrophys.*, *483*, L29–L33, doi:10.1051/0004-6361:200809761.
- Piccioni, G., L. Zasova, A. Migliorini, P. Drossart, A. Shakun, A. García Muñoz, F. P. Mills, and A. Cardesin-Moinelo (2009), Near-IR oxygen nightglow observed by VIRTIS in the Venus upper atmosphere, *J. Geophys. Res.*, *114*, E00B38, doi:10.1029/2008JE003133.
- Rengel, M., P. Hartogh, and C. Jarchow (2008), Mesospheric vertical thermal structure and winds on Venus from HHSMT CO spectral-line observations, *Planet. Space Sci.*, *56*, 1368–1384, doi:10.1016/j.pss.2008.07.004.
- Roldán, C., M. A. López-Valverde, M. López-Puertas, and D. P. Edwards (2000), Non-LTE Infrared Emissions of CO<sub>2</sub> in the Atmosphere of Venus, *Icarus*, *147*, 11–25, doi:10.1006/icar.2000.6432.
- Sánchez-Lavega, A., et al. (2008), Variable winds on Venus mapped in three dimensions, *Geophys. Res. Lett.*, *35*, L13204, doi:10.1029/2008GL033817.
- Sander, S. P., et al. (2003), Chemical kinetics and photochemical data for use in atmospheric studies, Evaluation 14, *JPL Publ.*, 02-25.
- Schofield, J. T., and F. W. Taylor (1983), Measurements of the mean, solar-fixed temperature and cloud structure of the middle atmosphere of Venus, *Q. J. R. Meteorol. Soc.*, *109*, 57–80, doi:10.1002/qj.49710945904.
- Schubert, G., et al. (1980), Structure and circulation of the Venus atmosphere, *J. Geophys. Res.*, *85*, 8007–8025, doi:10.1029/JA085iA13p08007.
- Schubert, G., S. W. Bougher, A. D. Covey, C. C. Del Genio, A. S. Grossman, J. L. Hollingsworth, S. S. Limaye, and R. E. Young (2007), Venus atmosphere dynamics: A continuing enigma, in *Exploring Venus as Terrestrial Planet*, *Geophys. Monogr. Ser.*, vol. 176, edited by L. W. Esposito, E. R. Stofan, and T. E. Cravens, pp. 121–138, AGU, Washington, D. C.
- Scott, G. B. I., D. A. Fairley, C. G. Freeman, M. J. McEwan, and V. G. Anicich (1998), Gas-phase reactions of some positive ions with atomic and molecular nitrogen, *J. Chem. Phys.*, *109*, 9010–9014, doi:10.1063/1.477571.
- Seiff, A., and D. B. Kirk (1982), Structure of the Venus mesosphere and lower thermosphere from measurements during entry of the Pioneer Venus probes, *Icarus*, *49*, 49–70, doi:10.1016/0019-1035(82)90056-2.
- Seiff, A., J. T. Schofield, A. J. Kliore, F. W. Taylor, and S. S. Limaye (1985), Models of the structure of the atmosphere of Venus from the surface to 100 kilometers altitude, *Adv. Space Res.*, *5*, 3–58, doi:10.1016/0273-1177(85)90197-8.
- Shah, K. P., D. O. Muhleman, and G. L. Berge (1991), Measurement of winds in Venus' upper mesosphere based on Doppler shifts of the 2.6-mm <sup>12</sup>CO line, *Icarus*, *93*, 96–121, doi:10.1016/0019-1035(91)90167-R.
- Soret, L., J. C. Gérard, A. Saglam, G. Piccioni, and P. Drossart (2009), Latitudinal-local time distribution of the O<sub>2</sub> and OH infrared nightglows and O density in the Venus lower thermosphere, paper presented at European Planetary Science Congress, Potsdam, German. (Available at <http://meetings.copernicus.org/epsc2009>.)
- Soret, L., J. C. Gérard, G. Piccioni, and P. Drossart (2010), Venus OH nightglow distribution from VIRTIS limb observations from Venus Express, *Geophys. Res. Lett.*, *37*, L06805, doi:10.1029/2010GL042377.
- Soret, L., J. C. Gérard, F. Montmessin, G. Piccioni, P. Drossart, and J.-L. Bertaux (2011), Atomic oxygen on the Venus nightside: Global distribution deduced from airglow mapping, *Icarus*, doi:10.1016/j.icarus.2011.03.034, in press.
- Sornig, M., T. Livengood, G. Sonnabend, P. Kroetz, D. Stupar, T. Kostiuik, and R. Schieder (2008), Venus upper atmosphere winds from ground-based heterodyne spectroscopy of CO<sub>2</sub> at 10  $\mu\text{m}$  wavelength, *Planet. Space Sci.*, *56*, 1399–1406, doi:10.1016/j.pss.2008.05.006.
- Stepanova, G. I., and G. M. Shved (1985), Radiative transfer in the 4.3- $\mu\text{m}$  CO<sub>2</sub> and 4.7- $\mu\text{m}$  CO bands in the non-LTE Venus and Mars atmospheres: Transformation of absorbed solar energy, *Sov. Astron., Engl. Transl.*, *29*, 528–530.
- Stewart, A. I., and C. A. Barth (1979), Ultraviolet night airglow of Venus, *Science*, *205*, 59–62, doi:10.1126/science.205.4401.59.
- Stewart, A. I. F., J. Gerard, D. W. Rusch, and S. W. Bougher (1980), Morphology of the Venus ultraviolet night airglow, *J. Geophys. Res.*, *85*, 7861–7870, doi:10.1029/JA085iA13p07861.
- Svedhem, H., D. Titov, F. Taylor, and O. Witasse (2009), Venus Express mission, *J. Geophys. Res.*, *114*, E00B33, doi:10.1029/2008JE003290.
- Vejby-Christensen, L., D. Kella, H. B. Pedersen, and L. H. Andersen (1998), Dissociative recombination of NO<sup>+</sup>, *Phys. Rev. A*, *57*, 3627–3634, doi:10.1103/PhysRevA.57.3627.
- von Zahn, U., K. H. Fricke, H. Hoffmann, and K. Pelka (1979), Venus: Eddy coefficients in the thermosphere and the inferred helium content of the lower atmosphere, *Geophys. Res. Lett.*, *6*, 337–340, doi:10.1029/GL006i005p00337.
- Widemann, T., E. Lellouch, and J. Donati (2008), Venus Doppler winds at cloud tops observed with ESPaDOnS at CFHT, *Planet. Space Sci.*, *56*, 1320–1334, doi:10.1016/j.pss.2008.07.005.
- Yung, Y. L., and W. B. Demore (1982), Photochemistry of the stratosphere of Venus: Implications for atmospheric evolution, *Icarus*, *51*, 199–247, doi:10.1016/0019-1035(82)90080-X.
- Zasova, L. V., V. I. Moroz, V. M. Linkin, I. V. Khatuntsev, and B. S. Maiorov (2006), Structure of the Venusian atmosphere from surface up to 100 km, *Cosmic Res., Engl. Transl.*, *44*, 364–383, doi:10.1134/S0010952506040095.
- Zhang, S., S. W. Bougher, and M. J. Alexander (1996), The impact of gravity waves on the Venus thermosphere and O<sub>2</sub> IR nightglow, *J. Geophys. Res.*, *101*, 23,195–23,205, doi:10.1029/96JE02035.

S. W. Bougher, A. S. Brecht, and C. D. Parkinson, Department of Atmospheric, Oceanic, and Space Sciences, University of Michigan, Space Research Building, 2455 Hayward St., Ann Arbor, MI 48109, USA. (bougher@umich.edu; abrecht@umich.edu; theshire@umich.edu)

B. Foster, High Altitude Observatory, National Center for Atmospheric Research, PO Box 3000, Boulder, CO 80307, USA. (foster@ucar.edu)

J.-C. Gérard, Laboratoire de Physique Atmosphérique et Planétaire, Institut d'Astrophysique et Géophysique, Université de Liège, Allée du 6 aout, 17, B-4000, Liège, Belgium. (JC.Gerard@ulg.ac.be)

S. Rafkin, Planetary Atmospheres and Surfaces, Department of Space Studies, Southwest Research Institute, Boulder, CO 80302, USA. (rafkin@boulder.swri.edu)